Centriole elimination during *C. elegans* oogenesis initiates with loss of the central tube protein SAS-1

Marie Pierron, Alexander Woglar, Coralie Busso, Keshav Jha, Tamara Mikeladze-Dvali[1], Marie Croisier[2], Pierre Gönczy

Swiss Institute for Experimental Cancer Research (ISREC), School of Life Sciences, Swiss Federal Institute of Technology Lausanne (EPFL), Lausanne, Switzerland

[1] Biocenter, Ludwig-Maximilians-University Munich, 82152 Planegg-Martinsried, Germany

[2] BIO-EM platform, School of Life Sciences, Swiss Federal Institute of Technology Lausanne (EPFL), Lausanne, Switzerland

Correspondence: pierre.gonczy@epfl.ch

KEY WORDS
Centriole elimination, oogenesis, *C. elegans,* electron microscopy, expansion microscopy, SAS-1

ABSTRACT

Centrioles are lost during oogenesis in most metazoans, ensuring that the zygote is endowed with the correct number of two centrioles, which are paternally contributed. How centriole architecture is dismantled during oogenesis is not understood. Here, we analyze with unprecedent detail the ultrastructural and molecular changes during oogenesis centriole elimination in *C. elegans*. Centriole elimination begins with loss of the so-called central tube and organelle widening, followed by microtubule disassembly. The resulting cluster of centriolar proteins then disappears gradually, usually moving in a microtubule- and dynein-dependent manner to the plasma membrane. Moreover, we find that neither Polo-like kinases nor the PCM, which modulate oogenesis centriole elimination in *Drosophila*, do so in *C. elegans*. Furthermore, we demonstrate that the central tube protein SAS-1 normally departs first from the organelle, which loses integrity earlier in *sas-1* mutants. Overall, our work provides novel mechanistic insights regarding the fundamental process of oogenesis centriole elimination.

INTRODUCTION

Centrioles are small evolutionary conserved organelles characterized by a nine-fold radially symmetric arrangement of microtubules (reviewed in (Bornens, 2012; Gomes Pereira et al., 2021; Winey and O'Toole, 2014)). Centrioles play a crucial role as templates for the axoneme of cilia and flagella, which are critical for cell signaling and motility. A pair of centrioles surrounded by the pericentriolar material (PCM) constitutes the centrosome, the principal microtubule organizing center (MTOC) of animal cells. The number of centrioles is tightly regulated. Most proliferating cells are born with two centrioles, each of which then seeds the assembly of a procentriole during S-phase, leading to four centrioles during mitosis, two per spindle pole. Improper centriole number leads notably to defective spindle assembly and aberrant chromosome segregation, which can result in developmental failure and tumor progression.(reviewed in (Nigg and Holland, 2018)) How the rules governing centriole number control are tuned to serve specific physiological contexts is poorly understood.

Centriole number control must be modified at fertilization to ensure that the two gametes together contribute a total of two centrioles to the zygote. This requirement is achieved in most metazoan organisms by inactivating or eliminating maternally-derived centrioles and providing two centrioles from the sperm (reviewed in (Delattre and Gönczy, 2004; Manandhar et al., 2005)). There are two principal removal modes of maternally-derived centrioles. In the first mode, maternal centrioles are removed following the meiotic divisions (Crowder et al., 2015). This is the case in starfish, for example, where centrioles are present at spindle poles during the two female meiotic divisions, such that three maternal centrioles are eliminated through polar body extrusion, with the last one being removed in the zygote (Borrego-Pinto et al., 2016; Pierron et al., 2020; Shirato et al., 2006; Sluder et al., 1993a, 1993b). In the second and most prevalent mode, which occurs notably in worms, flies and vertebrates, maternal centrioles are removed during oogenesis, before the meiotic divisions. A mechanism underlying this removal mode has been uncovered in *Drosophila*, where loss of the Polo kinase from centrosomes during oogenesis results in PCM disassembly and subsequent loss of focused centriolar proteins (Pimenta-Marques et al., 2016). In *C. elegans*, depletion of the RNA helicase CGH-1 or the TRIM-NHL protein LIN-41 delays, but does not abolish, oogenesis centriole elimination, as deduced from the prolonged persistence of foci containing centriolar proteins (Matsuura et al., 2016; Mikeladze-Dvali et al., 2012).

67 Importantly, the studies to date did not explain how these molecular players results in
68 centriole disassembly, nor did they assess organelle integrity at the ultrastructural level.
69 Analysis by electron-microscopy (EM) is critical to ensure that foci bearing centriolar proteins
70 correspond to *bona fide* centrioles. This is exemplified by the situation in mice, where foci
71 bearing the centriolar marker Centrin2::GFP are present at the poles of the female meiotic
72 spindle until metaphase II, despite centrioles being absent as judged by EM (Simerly et al.,
73 2018). Overall, despite being of fundamental importance for successful sexual reproduction,
74 centriole alterations during oogenesis have not been analyzed in detail at the ultrastructural
75 level, and understanding of the mechanisms governing this process is incomplete.

76 By contrast to the paucity of information regarding the sequence of events and the
77 mechanisms underlying oogenesis centriole elimination, substantial knowledge has been
78 accrued regarding the evolutionary conserved proteins that assemble the organelle (reviewed
79 in (Banterle and Gönczy, 2017; Gomes Pereira et al., 2021; Nigg and Holland, 2018; Ohta et
80 al., 2017)). In *C. elegans*, the first components recruited to the assembly site are the
81 interacting proteins SAS-6 and SAS-5, which form a so-called inner tube, the equivalent of the
82 cartwheel hub in other systems. SAS-6/SAS-5 recruitment requires the function of the ZYG-1
83 kinase, as well as the presence of SAS-7 and SPD-2 on the pre-existing centriole. Next comes
84 SAS-4, which is thought to facilitate the processive elongation of the microtubule singlets that
85 are then added to complete organelle assembly. The precise localization of 12 centriolar and
86 PCM core components has been uncovered in meiosis prophase I using Ultrastructure-
87 Expansion coupled to STED super-resolution microscopy (U-Ex-STED), enabling also the
88 mapping of these proteins onto specific ultrastructural elements defined by EM (Fig. 1A)
89 (Woglar et al., 2022). This work established notably that the microtubule interacting protein
90 SAS-1 localizes to the so-called central tube, a circular element between the SAS-6/SAS-5-
91 containing inner tube and microtubules. *sas-1* is dispensable for centriole assembly, but
92 essential to maintain stability of sperm-contributed centrioles in the zygote and of centrioles
93 during subsequent embryogenesis (von Tobel et al., 2014). Furthermore, the U-Ex-STED map
94 showed that the centriolar proteins HYLS-1, SPD-2, as well as the PCM core components
95 PCMD-1 and SPD-5, all localize peripheral to the microtubules, onto the so-called
96 paddlewheels (Woglar et al., 2022). The centriolar protein SAS-7, as well as the PCM
97 component γ-tubulin (TBG-1), localize more externally still. TBG-1, together with its
98 interactors GIP-1 and GIP-2, as well as its partner MZT-1, is present in the PCM core during

99 interphase, with more protein being present during mitosis, thereby enabling robust
100 microtubule nucleation. Other proteins, including the ZYG-9/TAC-1 complex, PLK-1 and the
101 Aurora A kinase AIR-1, contribute to centrosome maturation and microtubule nucleation
102 during mitosis (reviewed in (Pintard and Bowerman, 2019)).

103 *C. elegans* oocytes are produced in an assembly line fashion that provides access to all
104 stages of the centriole elimination process within a single gonad in a spatial-temporal gradient
105 (Fig. 1B)(Lints and Hall, 2004; Pazdernik and Schedl, 2013). Germ cell nuclei are produced in
106 the mitotic zone located in the distal end of the gonad. Nuclei then progress towards the
107 proximal end, going through early prophase, late pachytene and then diplotene of meiosis I,
108 before undergoing cellularization after the loop region, yielding oocytes that then mature
109 further. Fertilization occurs as fully mature oocytes pass through the spermatheca and
110 execute the two meiotic divisions without maternal centrioles. Prior analysis of *C. elegans*
111 oogenesis centriole elimination using antibodies against centriolar and PCM proteins, as well
112 as transgenic worms expressing fusion proteins, combined with serial-section EM of a few
113 cells, uncovered that centrioles are eliminated during diplotene (Mikeladze-Dvali et al., 2012).
114 However, the sequence of ultrastructural changes during centriole elimination has not been
115 addressed in this initial study. Moreover, the prior work was conducted before the advent of
116 expansion microscopy, which holds the potential to provide high spatial resolution
117 information on changes in molecular architecture during this process.

118 Here, we set out to investigate in more depth the mechanisms underlying centriole
119 elimination during *C. elegans* oogenesis. We conducted live imaging of endogenously tagged
120 centriolar and PCM core proteins, including in a microfluidic device enabling long term
121 monitoring. We uncovered that the signal intensity of centriolar protein foci starts to diminish
122 in diplotene, but remains detectable in maturing oocytes, where it usually moves to the
123 plasma membrane. Moreover, we established that neither the Polo like kinases PLK-1, PLK-2
124 and PLK-3, nor the PCM, protects centrioles from elimination in *C. elegans* oogenesis.
125 Furthermore, combining Correlative Light Electron Microscopy (CLEM) with U-Ex-STED, we
126 uncovered discrete changes in centriole architecture during centriole elimination, and
127 correlated them with corresponding alterations in protein abundance. In particular, we found
128 that the initial step of elimination is marked by the departure of SAS-1 from the centriole and
129 an increase of organelle diameter. Moreover, we show that SAS-1 plays a critical role in timing
130 centriole elimination during worm oogenesis.

131

132 **RESULTS**

133 **Progressive loss of centriolar and PCM protein foci**

134 We set out to analyze the process of centriole elimination during *C. elegans* oogenesis in new
135 detail. First, we investigated whether centriolar and PCM proteins are removed at the same
136 time or instead in a sequence that may be indicative of the underlying mechanism. To this
137 end, we utilized worm strains simultaneously expressing fluorescently tagged endogenous
138 SAS-7 and a tagged version of another centriolar or PCM protein expressed from the
139 endogenous locus or as a validated transgene (Table 1). We performed live confocal imaging
140 of young adult hermaphrodites, quantifying fluorescence intensities in foci enriched in
141 centriolar or PCM proteins from the diplotene stage in the loop region until the last oocyte
142 before the spermatheca (Fig. 1; Fig. S1). Note that by convention oocytes are numbered
143 according to their position relative to the spermatheca, with the most proximal one referred
144 to as the -1 oocyte (Fig. 1B). We found that the fluorescence intensity of foci enriched in
145 centriolar or PCM proteins associated with each germ cell nucleus starts to decay in diplotene,
146 typically in the -10 oocyte (Fig. 1 D, F, H, J). Moreover, we found dimmer foci as far as the -2
147 oocyte for the centriolar proteins SAS-6, SAS-4, SAS-7 and HYLS-1 (Fig. 1C, 1G; Fig. S1A). The
148 same was true for the PCM core components SPD-2, SPD-5 and PCMD-1, as well as the γ-
149 tubulin-interacting proteins GIP-1 and MZT-1 (Fig. 1E, 1I; Fig. S1B-D). Overall, we conclude
150 that all centriolar and PCM core proteins analyzed diminish in intensity starting approximately
151 in the -10 oocyte, but remain detectable in a focus until later.

152 We next analyzed fluorescence intensity decay of proteins in the focus with respect to
153 SAS-7, which served as a standard in all animals. With the exception of SPD-5 and SAS-6, we
154 found that focused fluorescence intensity decreases similarly for SAS-7 and the other proteins
155 analyzed, indicating concomitant decay (Fig. 1D, 1F; Fig. S1A-S1D). In the case of SAS-6, the
156 cytoplasm of -6 to -1 oocytes contains many dim foci (Fig. 1G), which prevents one from
157 thoroughly assessing whether a focus of centriolar SAS-6 persists after disappearance of the
158 SAS-7 focus, although slower decay of SAS-6 fluorescence levels suggests that this might be
159 the case (Fig. 1H). By contrast, we found that the PCM core protein SPD-5 is removed earlier
160 than SAS-7 (Fig. 1I, 1J). Furthermore, MZT-1 and GIP-1 remain present in a focus in maturing
161 oocytes despite the absence of SPD-5 (Fig. S1C, S1D), which is different from the situation in
162 embryos, where SPD-5 is required for γ-tubulin recruitment to centrosomes (Hamill et al.,

163 2002). We also found that centrosomal AIR-1 and ZYG-9 are present only in mitotic cells in
164 the distal region of the gonad, but not thereafter (Fig. S1E, S1F), as anticipated from their
165 recruitment to mature centrosomes in the early embryo (Matthews et al., 1998; Schumacher
166 et al., 1998), as well as from analogous distributions in other systems (Crosio et al., 2002; Giet
167 et al., 2002).

168 Together, these data reveal that the removal of centriolar and PCM proteins occurs
169 progressively during oogenesis, starting in diplotene of meiotic prophase I and finishing in
170 mature oocytes. Most proteins depart in a concomitant manner, except for SPD-5, which is
171 removed earlier, and SAS-6, which appears to be removed later.

172

173 **Foci containing centriolar proteins detach from the nucleus and move to the plasma**
174 **membrane in a microtubule- and dynein-dependent manner**

175 Whilst analyzing the distribution of centriolar and PCM core protein foci, we noticed that
176 instead of residing in the vicinity of the nucleus, as is usually the case for centrioles, such foci
177 are sometimes present in the cytoplasm or at the plasma membrane, in particular in the last
178 few oocytes (see Fig. S1A, -5 oocyte, and Fig. S1B, -3 oocyte). To investigate this phenomenon
179 further, we utilized a microfluidic device designed for long-term non-invasive imaging of
180 *C. elegans*, allowing us to track the focus of centriolar proteins for hours (Berger et al., 2018).
181 We performed 4D widefield live imaging of gonads expressing RFP::SAS-7 and MEL-28::GFP,
182 a nucleoporin localized at the nuclear envelope (Galy et al., 2006), or else expressing RFP::SAS-
183 7 and RME-2::GFP, a yolk receptor enriched at the plasma membrane of the most mature
184 oocytes (Grant and Hirsh, 1999)(Fig. 2A; see Materials and methods). We imaged 11 gonads,
185 starting with oocytes situated in positions -6 to -4 at the onset of the experiment, following
186 them for 3-5 hours during their progression towards the spermatheca. This analysis
187 established that in ~80% of cases (26/33 oocytes), the RFP::SAS-7 focus detaches from the
188 nuclear envelope (Fig. 2A, 0'), and moves towards the plasma membrane (Fig. 2A, 52'). The
189 focus persists in that location during oocyte enlargement (Fig. 2A, 156'), before becoming
190 undetectable (Fig. 2A, 166'). We generated kymographs from 7 movies in which the focus of
191 RFP::SAS-7 remained largely in the XY imaging axis, finding an average velocity of
192 ~0.65μm/min (Fig. 2B, 2C) (see Discussion).

193 What could cause movement of the RFP::SAS-7 focus towards the plasma membrane?
194 Protein aggregates are known to move within mature oocytes before being degraded via a

195 sperm-derived signal (Adam Bohnert and Kenyon, 2017). However, we found that RFP::SAS-7
196 foci movement was not altered in feminized mutant animals lacking sperm (Fig. S2A-S2D).
197 Moreover, we investigated whether the PCM could facilitate juxtanuclear retention of
198 RFP::SAS-7 foci. Compatible with this notion, centriolar foci detach prematurely from germ
199 cell nuclei in *pcmd-1(t3421ts)* mutant animals, which fail to assemble PCM (Erpf et al., 2019);
200 as a result, centriolar foci devoid of nuclei are present in the gonad rachis and the loop region
201 (Fig. 2D, 2E). This finding suggests that the PCM contributes to linking centrioles to the nuclear
202 envelope. In turn, this may explain why RFP::SAS-7 foci normally depart from the nuclear
203 envelop after the loop region, where SPD-5 levels decrease substantially (see Fig. 1I, 1J).
204 Next, we used RNAi in worms expressing RFP::SAS-7 and RME-2::GFP to test whether
205 microtubule and F-actin, as well as molecular motors, are required for focus movement
206 towards the plasma membrane. To increase throughput, we imaged worms at a single time
207 point, assessing whether centriolar foci were juxtanuclear or not in -12 to -1 oocytes (Fig. 2F-
208 2K; Fig. S2E-S2I). In line with the live imaging observations, we found that centriolar foci were
209 present in the cytoplasm in approximately 50% of -7 oocytes in the control condition (Fig. 2F,
210 2G). No change was observed either upon F-actin depletion, despite modifications of gonad
211 architecture following *act-1*(*RNAi*) (Fig. S2E, S2F). In stark contrast, depletion of microtubules
212 through *tba-2*(*RNAi*), as well as of the dynein heavy chain DHC-1 or the dynein light chain
213 DLC-1, essentially abrogated movement, with RFP::SAS-7 foci almost invariably remaining at
214 the nuclear envelope (Fig. 2H-2K; Fig. S2G). Depletion of the conventional kinesin UNC-116
215 led to a milder reduction (Fig. S2H, S2I). Therefore, microtubules and dynein are required for
216 RFP::SAS-7 focus movement to the plasma membrane, with kinesin contributing as well.
217 Overall, our findings uncover that oogenesis centriole elimination in *C. elegans*
218 comprises a late phase during which the focus containing diminishing levels of centriolar and
219 PCM proteins can detach from the nucleus and move towards the plasma membrane in a
220 microtubule- and dynein-dependent manner. Importantly, however, in approximately 20% of
221 oocytes, the focus of RFP::SAS-7 becomes undetectable in the vicinity of the nucleus, without
222 apparent movement towards the plasma membrane. Moreover, when microtubules or
223 dynein components were depleted, RFP::SAS-7 centriolar foci eventually disappeared (see
224 Fig. 2I, 2K, grey lines), despite the absence of plasma membrane-directed movement.
225 Therefore, even if frequent in the control condition, this phenomenon is not essential for the
226 clearance of foci with centriolar and PCM proteins during *C. elegans* oogenesis.

227 **Depletion of Polo-like kinases or PCM removal does not lead to precocious centriole**
228 **elimination during *C. elegans* oogenesis**
229 Given that Polo-mediated PCM removal triggers oogenesis centriole elimination in the fly
230 (Pimenta-Marques et al., 2016), we investigated whether Polo-like kinases and the PCM
231 operate similarly in the worm. There are three Polo-like kinases in *C. elegans*: PLK-1, which is
232 essential and closest to Polo, exerting analogous functions during centrosome maturation and
233 embryonic cell division (Chase et al., 2000); PLK-2, which is not essential and functions in
234 meiotic chromosome organization (Brandt and Kim, 2021); the more divergent and non-
235 essential PLK-3, which has no ascribed function. Previous immunostaining established that
236 PLK-1 and PLK-2 in the gonad localize at centrosomes exclusively in the mitotic zone (Harper
237 et al., 2011). Accordingly, we found that endogenously tagged PLK-1::GFP marks centrosomes
238 exclusively in dividing cells in that region (Fig. 3A).
239 In principle, PLK-1 could be present below detection levels in later stages when
240 elimination occurs, or exerts a function in the mitotic zone that translates into subsequent
241 organelle elimination. To explore these formal possibilities, we set out to investigate the role
242 of PLK-1, as well as PLK-2 and PLK-3 in case redundancies were at play. We used *plk-1(RNAi)*
243 feeding conditions that result in meiotic arrest (Budirahardja and Gönczy, 2008), as well as
244 the null alleles *plk-2*(*ok1936*) and *plk-3*(*gk1103*). All analyzed animals expressed RFP::SAS-7
245 and RME-2::GFP to score centriolar focus disappearance relative to oocyte maturation, using
246 the presence of RME-2::GFP on the plasma membrane to this end (Materials and methods).
247 Importantly, we found that the timing of RFP::SAS-7 centriolar focus elimination is
248 comparable in *plk-1(RNAi)* animals and control worms, with ~70% of -3/-4 oocytes harboring
249 both RFP::SAS-7 foci and RME-2::GFP (Fig. 3B-3E). In *plk-2*(*ok1936*) mutant gonads, oocyte
250 maturation occurs earlier than in the control, as evidenced by the presence of RME-2::GFP
251 positive oocyte as early as positions -12/-11 (Fig. 3F, 3G). RFP::SAS-7 foci are also sometimes
252 lost earlier, but the concordance between RME-2::GFP rise and RFP::SAS-7 decay is preserved,
253 demonstrating that the timing of elimination is not altered (Fig. 3G). When PLK-1 is depleted
254 by RNAi in *plk-2*(*ok1936*) animals, oocyte maturation is even more precocious, but RFP::SAS-
255 7 disappearance still occurs after RME-2::GFP increase (Fig. 3H, 3I). Finally, *plk-1(RNAi) plk-*
256 *2*(*ok1936*) *plk-3*(*gk1103*) triply inactivated animals do not exhibit additional phenotypes
257 regarding oocyte maturation or centriole elimination timing (Fig. 3J, 3K).

258 Because RNAi-mediated depletion can sometimes be incomplete, we combined
259 *plk-2(ok1936)* with the thermosensitive allele *plk-1(or683ts)* at the restrictive temperature to
260 achieve the strongest possible depletion condition compatible with life. This yielded highly
261 disorganized gonads, yet with seemingly normal centriole elimination timing, as SPD-2 and
262 SPD-5 foci persist until the RME-2::GFP signal appears, as in control worms (Fig. S3A, S3B). In
263 order to further test whether centriole elimination in *plk-2(ok1936) plk-1(or683ts)* animals
264 correlates with oocyte maturation, we immunostained gonads with IFA-1 pan-centriolar
265 antibodies and counterstained them with a DNA dye to assess chromosome condensation as
266 a proxy for meiotic progression (see Fig. 1B) (Phillips et al., 2009). We found in both control
267 and mutant worms that centriolar foci are present in the vicinity of nuclei with chromosomes
268 characteristic of the late diplotene stage (Fig. S3C, S3D). Overall, we conclude that Polo-like
269 kinases do not modulate centriole elimination timing in *C. elegans*.
270 We next tested whether the PCM may be required for centriole stability
271 independently of PLK-1, PLK-2 and PLK-3. PCMD-1 is essential for generating the PCM core
272 (Erpf et al., 2019), and we therefore utilized the strong *pcmd-1*(*t3421ts*) mutant allele at the
273 restrictive temperature to test whether PCM removal results in premature loss of centriolar
274 foci. Importantly, we found that although RFP::SPD-5 was absent from centrosomal foci
275 during oogenesis in *pcmd-1*(*t3421ts*) animals, as anticipated from findings in the embryo (Erpf
276 et al., 2019), the kinetics of GFP::SAS-7 or SAS-4 loss were not altered (Fig. 4A-C; Fig. S3E, S3F).
277 Moreover, we found that GFP::SAS-7 decay in such animals coincides with RME-2::GFP
278 enrichment, further demonstrating that elimination timing is not impacted in the absence of
279 SPD-5 (Fig. 4D). We conclude that PCM loss does not lead to precocious loss of foci with
280 centriolar and PCM core proteins during *C. elegans* oogenesis.
281
282 **Central tube loss and centriole widening mark the onset of centriole elimination**
283 We performed CLEM to characterize the centriole elimination process at the ultrastructural
284 level to gain insights into the mechanisms leading to organelle removal. We dissected, fixed
285 and imaged two gonads expressing GFP::SAS-7, followed by resin embedding and 50 nm serial
286 section EM analysis. A total of 69 foci bearing GFP::SAS-7 were analyzed in this manner,
287 representing successive stages of oogenesis and, therefore, centriole elimination. Each
288 nucleus with an accompanying GFP::SAS-7 focus was first visualized by brightfield and then
289 identified in the corresponding serial sections, thus providing spatial coordinates to spot

290 centrioles (Fig. 5A-5C). As previously reported (Mikeladze-Dvali et al., 2012; Woglar et al.,
291 2022), we found that nuclei in early meiotic prophase possess four centriolar units, two
292 mature centrioles and two associated procentrioles (Fig. 5D). Distinct ultrastructural elements
293 can be observed in top views at this stage, including the inner-most tube, the central tube,
294 microtubule singlets, and the peripheral-most paddlewheel (Fig. 5E) (Sugioka et al., 2017;
295 Woglar et al., 2022). Strikingly, during diplotene, which corresponds approximately to when
296 the intensity of the GFP::SAS-7 focus begins to decline (see Fig. 1), ultrastructural analysis
297 revealed that the central tube is no longer detectable (Fig. 5F). In addition, this is
298 accompanied by an increase of organelle diameter (Fig. 5I, 5J). Loss of centriole integrity was
299 observed thereafter, with microtubule singlets no longer being recognized (Fig. 5G), which
300 was followed by the complete loss of a detectable centriole (Fig. 5H). Interestingly, this is the
301 case despite GFP::SAS-7 remaining present in a focus at this stage, which will be cleared
302 eventually as reported above.
303 Taken together, these results reveal that centriole elimination during *C. elegans*
304 oogenesis is characterized by an initial loss of organelle integrity, followed by loss of an
305 amorphous cluster of centrosomal proteins. Moreover, these findings raise the possibility that
306 the first observable ultrastructural alteration, namely central tube removal, may cause
307 subsequent loss of centriole integrity.
308
309 **U-Ex-STED reveals that SAS-1 leaves centrioles at the onset of centriole elimination**
310 U-Ex-STED analysis of gonad centrioles established that the central tube harbors the
311 microtubule-binding protein SAS-1 (Woglar et al., 2022). Suggestively, SAS-1 is required for
312 the stability of sperm-derived centrioles in the zygote and of centrioles assembled
313 subsequently during embryogenesis (von Tobel et al., 2014). Together with our finding that
314 central tube loss is a hallmark of centriole elimination onset during oogenesis, this raises the
315 possibility that SAS-1 removal may mark the first step of organelle removal in the female
316 germline. To investigate this possibility, we used U-Ex-STED to analyze the distribution of
317 endogenously tagged SAS-1::3xFLAG during the course of the changes uncovered by EM, in
318 relationship to SAS-7 and SAS-4 distribution. Since the central tube is the first ultrastructural
319 element to vanish, we expected fluorescence intensity of the SAS-1 focus to diminish before
320 that of SAS-7 and SAS-4, and found this to be the case indeed (Fig. 6A-6C). We used U-Ex-STED
321 to refine the timing of SAS-1 loss relative to that of microtubules, finding that GBP::RFP::SAS-

322 1 fluorescence at centrioles decays faster than that of microtubules, consistent with the early
323 loss of the central tube observed by EM (Fig. 6D, 6G). Using an analogous experimental
324 strategy, we set out to investigate the integrity of other ultrastructural elements in
325 relationship to microtubules. Importantly, whereas SPD-5 rings are dismantled concomitantly
326 with microtubule singlets (Fig. S4A, S4B), consistent with the early loss of SPD-5 uncovered in
327 live specimens (see Fig. 1I, 1J), we found that centriolar microtubules are lost before SPD-2 or
328 SAS-4 (Fig. 6E-6G). This finding likely explains why foci containing centriolar proteins with
329 decaying signal intensity remain present in maturing oocytes despite the complete loss of
330 ultrastructural integrity observed by EM (Fig. 5H). Moreover, like in the EM analysis, U-Ex-
331 STED uncovered a widening of centrioles as they progress through meiosis, as evidenced by
332 measurements of SPD-2, microtubules and SAS-4 ring diameters (Fig. 5H).
333 Together, these data demonstrate that removal of the microtubule-binding protein
334 SAS-1 is an early event in the sequence of events leading to organelle demise.
335
336 **SAS-1 is required for centriole structural integrity and stability during oogenesis**
337 If SAS-1 departure from centrioles not only marks the onset of oogenesis centriole
338 elimination, but is also important for this process to occur, then impairing *sas-1* function
339 should exacerbate loss of centriole integrity. To test this prediction, we performed U-Ex-STED
340 on gonads from the strong reduction-of-function allele *sas-1(t1521ts)* at the restrictive
341 temperature. Strikingly, we found that centrioles are as wide in early prophase as they are in
342 diplotene in this mutant background, whereas widening only occurs during diplotene in the
343 control (Fig. 7A-7C). Moreover, whereas SAS-4 is normally present in approximately equal
344 amounts next to each of the nine centriolar microtubules in early prophase, this is not the
345 case in *sas-1(t1521)* mutant animals, where intensities are more variable (Fig. 7D). Together,
346 these two data sets suggest that centriole integrity is already affected in early prophase when
347 *sas-1* function is compromised. Furthermore, U-Ex-STED analysis revealed that centriolar
348 microtubules and SAS-4 signals decay faster during meiosis progression in *sas-1(t1521ts)*
349 mutant animals than in the control (Fig. 7E, 7F). This is accompanied by premature loss of
350 organelle integrity, as evidenced by the fraction of centrioles in diplotene with less than nine
351 foci of centriolar SAS-4 and completely disorganized centrioles (Fig. 6G). Overall, these data
352 demonstrate that SAS-1 is required for centriole stability during oogenesis, and suggest that
353 SAS-1 departure from centrioles may trigger organelle elimination from the female germ line.

356 **DISCUSSION**

357 We established with precision the course of events leading to centriole elimination during
358 *C. elegans* oogenesis using multi-scale microscopy and molecular genetic approaches. We
359 discovered that oogenesis centriole elimination is characterized by an initial loss of the central
360 tube and organelle integrity, followed by the gradual disappearance of an amorphous cluster
361 of centrosomal proteins. The latter often occurs after detachment from the nucleus and
362 movement to the plasma membrane in a microtubule- and dynein-dependent manner,
363 although such movement is not essential for disappearance . Finally, we demonstrate that the
364 central tube protein SAS-1 is the first component to leave centrioles and propose that this
365 event triggers centriole elimination.

366

367 **Clearance of amorphous cluster of centrosomal proteins**

368 We found that, following the loss of centrioles recognizable by EM, an amorphous cluster
369 containing several centrosomal proteins persists up to the -2 oocyte, later than what was
370 previously reported (Matsuura et al., 2016; Mikeladze-Dvali et al., 2012). The prolonged
371 detection of foci in the present study probably reflects the use of brighter CRISPR/Cas9-based
372 and transgenic reporters, as well as more sensitive microscopy. Using live imaging, we show
373 that in ~80% of cases, cluster removal occurs after detachment from the nucleus and
374 movement to the plasma membrane in a microtubule- and dynein-dependent manner.
375 Whereas the centrosome is known to be linked to the nucleus in the embryo via ZYG-12/SUN-
376 1 (Malone et al., 2003; Zhou et al., 2009), the components mediating the analogous link in the
377 gonad are not known. Our findings suggest that SPD-5 and the PCM are involved. Indeed, in
378 the absence of these components upon *pcmd-1* inactivation, centrioles tend to detach from
379 nuclei already in early prophase, localizing to the rachis and the loop region. Moreover, in the
380 control condition, the SPD-5 focus is reduced to ~30% of initial levels already in -7 oocytes,
381 shortly before cluster detachment initiates, compatible with a causative link. Alternatively, a
382 more global remodeling of the nuclear envelope might promote detachment of different
383 molecular complexes in maturing oocytes since P-granules, which do not contain PCM
384 proteins, also detach from the nuclear envelope around that time (Spike et al., 2008).

385 Cluster movement to the plasma membrane occurs at an average velocity of
386 ~0.65μm/min, which is very slow considering that it relies on microtubules and dynein, and

387 partly on kinesin. Dynein and kinesin motor proteins in *C. elegans* exhibit velocities along
388 microtubules that are two orders of magnitude faster (Gönczy et al., 1999; Pierce et al., 1999).
389 Interestingly, centrioles also translocate in a microtubule- and dynein-dependent manner
390 from the nuclear vicinity to the tip of the dendrite in the PQR sensory neuron in *C. elegans*, a
391 movement that is accompanied by gradual loss of centriolar proteins (Li et al., 2017). Such
392 movement was proposed to result from transient interactions between dynein and centrioles
393 (Li et al., 2017), and it may be that the same mechanism is at play during oogenesis.
394 Alternatively, given that the microtubule network is nucleated mainly from the nuclear
395 envelope and the plasma membrane in *C. elegans* oocytes, with dynein being required for
396 overall network organization (Zhou et al., 2009), not having these components may lead to a
397 disorganized cellular state incompatible with cluster movement. Regardless, importantly, we
398 show that cluster movement to the plasma membrane is not essential for disappearance of
399 clustered centrosomal proteins, since ~20% of clusters remain in the vicinity of the nucleus
400 and yet are disposed of. Why should such a clearance step be needed when centriole integrity
401 has been lost already? It has been established notably in human cells that centriolar protein
402 assemblies that are not *bona fide* organelles, in that they do not harbor centriolar
403 microtubules, can nevertheless act as MTOCs, and thereby lead to faulty spindle assembly
404 (Balestra et al., 2021; Li et al., 2012; Shiratsuchi et al., 2015). Therefore, clearance of the
405 cluster of centrosomal proteins in *C. elegans* may serve as a safety mechanism to prevent
406 regaining MTOC activity in the oocyte and the zygote.
407
408 **Diversity in Polo-like kinase requirement for oogenesis centriole elimination**
409 Whereas Polo kinase and the PCM play a critical role in centriole elimination during
410 *Drosophila* oogenesis (Pimenta-Marques et al., 2016), we demonstrate that the situation
411 differs in *C. elegans*. Indeed, single or combined depletion of PLKs, as well as removal of the
412 PCM core component SPD-5, do not have a discernable impact on the timing of centriole
413 elimination in the worm. Whereas time-resolved analysis by serial-section EM would be
414 needed to ascertain that no change in centriole ultrastructure has occurred, several
415 considerations may explain the difference between the two systems. First, whereas Polo is
416 present at centrioles in the *Drosophila* germ line in ~40% of stages 7/8 oocytes and in ~15%
417 of stage 9/12 oocytes, when elimination occurs, PLK-1 and PLK-2 are located at centrioles only
418 in proliferating germ cells in *C. elegans*, much before elimination begins (Jaramillo-Lambert

419 et al., 2007; Mikeladze-Dvali et al., 2012). Second, whereas Polo is required to maintain the
420 PCM in fly oocytes, we show here that depleting PLKs in the worm has no impact on the timing
421 of loss of the PCM core protein SPD-5. Third, we note that 64 centrioles, 60 from the 15 nurse
422 cells plus 4 from the oocyte proper, end up clustered in the *Drosophila* oocyte(Pimenta-
423 Marques et al., 2016), whereas merely 4 centrioles are present in the vicinity of each germ
424 nucleus in the *C. elegans* gonad. Perhaps a large PCM surrounding a cluster of 64 centrioles
425 prevents the elimination machinery to reach centrioles in *Drosophila*, such that prior PCM
426 disassembly is a prerequisite for organelle removal. Inhibiting Plk1 in starfish oocytes does
427 not alter disappearance timing of foci bearing the centriolar marker Centrin2, suggesting that
428 also in this system centriole elimination is not regulated by this kinase (Pierron et al., 2020).
429 Future work should help clarify to what extent the requirement in *Drosophila* oogenesis is
430 deployed in other centriole elimination settings.
431
432 **Central tube and SAS-1 removal mark the onset of centriole elimination**
433 By combining EM and U-Ex-STED, we reveal that the first detectable sign of centriole
434 elimination is the disappearance of the central tube, together with a widening of the
435 centriole, which precede the loss of microtubule singlets and of organelle integrity. These
436 observations are partially reminiscent of the centriole degeneration steps at the time of cilium
437 formation in amphid neurons, with the loss of the inner core structure and the splaying of
438 microtubules (Doroquez et al., 2014; Nechipurenko et al., 2017; Serwas et al., 2017).
439 Moreover, the ~40nm increase of organelle diameter measured during that degeneration
440 process is in the range of that determined here during oogenesis centriole elimination
441 (Nechipurenko et al., 2017). However, as opposed to the early loss of SAS-6 and then SAS-4
442 in amphid neurons (Nechipurenko et al., 2017; Serwas et al., 2017), we find here that these
443 proteins persist until the end of centriole elimination during oogenesis.
444 Our analysis uncovered a critical role for SAS-1 during oogenesis centriole elimination.
445 We find that SAS-1 is the earliest component analyzed to depart from centrioles during this
446 process, in line it being a central tube component (Woglar et al., 2022). In addition, U-Ex-STED
447 analysis revealed that centrioles are as wide during early prophase as they are in diplotene in
448 *sas-1(t1521ts)* mutant animals. Moreover, centrioles in *sas-1(t1521ts)* mutants are
449 eliminated faster than in control conditions. Together, these findings define SAS-1 as a key
450 player in the initiation of centriole elimination.

451 SAS-1 was known already to be required for the stability of sperm-derived centrioles:
452 centrioles derived from *sas-1* mutant sperm lose their integrity shortly after fertilization, as
453 evidenced by the reduction of centriolar fluorescent markers intensity and ultrastructural
454 analysis (von Tobel et al., 2014). Moreover, centrioles assembled in embryos with
455 compromised *sas-1* function are likewise unstable (von Tobel et al., 2014). Interestingly, SAS-
456 1 associates with microtubules when expressed in human cells (von Tobel et al., 2014).
457 Combined with the U-Ex-STED data, these findings taken together suggest that the central
458 tube, and SAS-1 in particular, may act as an inner brace holding the microtubule singlets
459 together.
460 SAS-1 is an ortholog of the human ciliopathy protein C2CD3 (C2 domain containing 3),
461 which is involved in human centriole length control and organization of distal appendages,
462 where it forms a distal brace perhaps analogous to the worm central tube (Chang et al., 2023;
463 Gaudin et al., 2022; Thauvin-robinet et al., 2014). *C. elegans* centrioles lack apparent
464 proximal/distal polarity, with all constituent proteins known to date being homogeneously
465 distributed along its length. Whether C2CD3 plays a role in centriole stability in human cells
466 or may be targeted for disassembly in specific cellular context remains to be tested. Because
467 centrioles disassemble earlier in *sas-1* mutant without impacting oogenesis, a potential
468 involvement of C2CD3 in vertebrate oogenesis centriole elimination may have gone
469 undetected.
470 To conclude, our findings contribute to the understanding of centriole elimination
471 during oogenesis, a fundamental process that is essential for the sexual reproduction of
472 metazoan organisms. Furthermore, we anticipate the sequence of events unraveled here,
473 with the key role of SAS-1 at the onset of the elimination process, to serve as a platform to
474 understand centriole fate modulation in other physiological and pathological contexts.
475
476
477

478 **ACKNOWLEDGEMENTS**
479 We are grateful to the laboratories of Bruce Bowerman, Alex Dammermann, Jessica Feldman,
480 Anthony Hyman, Kevin O'Connell and Anne M. Villeneuve for their gift of worm strains. Some
481 other strains were provided by the *Caenorhabditis* Genetics Center (CGC), which is funded by
482 the NIH Office of Research Infrastructure Programs (P40 OD010440). We thank Graham Knott,
483 head of the BIO-EM platform, as well as Simon Berger for training with the microfluidic
484 chamber and providing the tools. We are grateful to Gabriela Garcia Rodriguez and Nils
485 Kalbfuss for comments on the manuscript, as well as to Léo Burgy for help with statistical
486 analysis. This work was funded by post-doctoral fellowships from EMBO to M.P. (ALTF 1426-
487 2016), the European Union to A. W. (MCSA-IF 588594) and DFG to T. M.-D. (MI1867/1-3), as
488 well as by grants to P.G. from the Novartis Foundation for Medical-Biological Research
489 (18C186) and the Swiss National Science Foundation (310030_197749).
490

491 **AUTHOR CONTRIBUTIONS**
492 Conceptualization, M.P., A.W., T.M-D., P.G.; Investigation, M.P., A.W., C.B., K.J., T. M-D.;
493 Writing – Original Draft, M.P., A.W., K.J. and P.G.; Funding Acquisition, M.P., A.W., P.G., T.M-
494 D; Supervision, P.G.
495

496 **DECLARATION OF INTERESTS**
497 The authors declare no competing interests.
498

499 **FIGURES LEGENDS**
500 **Figure 1. Progressive loss of foci enriched in centriolar and PCM components**
501 **A.** Schematic of a slightly tilted view of worm centriole, illustrating the distribution of select
502 centriolar and PCM components. The dimensions of meiotic prophase centrioles are ~140nm
503 in diameter x ~100 nm in height. Modified after (Woglar et al., 2022).
504 **B.** Schematic of an adult hermaphrodite gonad showing progression of germ cells from the
505 mitotic zone, through early meiotic prophase, late pachytene and then diplotene, before
506 cellularization into maturing oocytes. Oocytes are numbered in reverse order according to
507 their distance from the spermatheca. The most mature -1 oocyte will enter the spermatheca
508 where it is fertilized, thereby giving rise to the zygote. The condensation state of the
509 chromatin is schematized in blue. Not drawn to scale.

510 **C-J.** Gonads from synchronized worm populations expressing the indicated two markers (C, E,
511 G, I), together with corresponding fluorescence intensity quantifications (D, F, H, J, in arbitrary
512 units normalized to the maximal and minimal fluorescence intensity in analyzed oocytes in
513 each case ± SD). Here and in Fig.3, we measured the correlation for each pair of markers and
514 R^2 of fits are indicated together with N for each panel. (C, D): SAS-4::mCherry and GFP::SAS-
515 7, N=10 and R^2=0.98; (E, F): SPD-2::GFP and RFP::SAS-7, N=9 and R^2=0.98; (G, H): SAS-6::GFP
516 and RFP::SAS-7, N=10 and R^2=0.93; (I, J) RFP::SPD-5 and GFP::SAS-7, N=12 and R^2=0.84. Unless
517 stated otherwise, here and in all figures, images are max-intensity projections of relevant z-
518 slices from 3D confocal live imaging. Dashed white lines delineate the gonad and oocytes,
519 which are numbered as in B. Arrowheads point to the location of centriolar protein foci. Here,
520 as well as in Fig. 2 and Fig. 3, orange arrowheads point to foci that are not obvious in the
521 overview because they reside in deeper slices. Insets are 12 microns thick max-intensity
522 projections. Scale bars are indicated in a single image per Figure if all images are scaled
523 identically.
524
525 **Figure 2. Centriolar foci remnant detach from the nuclear envelope and move to the plasma**
526 **membrane in a microtubule- and dynein-dependent manner**
527 **A.** Widefield time lapse imaging of an oocyte initially located at position -6, which reaches
528 position -1 position by the end of the movie, from a worm immobilized in the microfluidic
529 device expressing MEL-28::GFP and RFP::SAS-7. Top: brightfield (BF); middle: merge between
530 MEL-28::GFP (green) and RFP::SAS-7 (magenta); bottom: magnified insets showing RFP::SAS-
531 7 focus indicated by an arrowhead at each time point. Brightfield images and MEL-28::GFP
532 signal were used to outline the plasma membrane and the nuclear envelope, respectively,
533 both marked with dashed lines. Note RFP::SAS-7 centriolar focus detaching from the nuclear
534 envelope (0'), moving to the plasma membrane (0'-52'), and persisting there during oocyte
535 enlargement (156'), before disappearing (166'). Time in minutes. See also Movie S1.
536 **B.** Kymograph from widefield time-lapse imaging in A and Movie S1, showing movement of
537 the RFP::SAS-7 focus (magenta) away from the nuclear envelope (ne) towards the plasma
538 membrane (pm) (I.). Note that the RFP::SAS-7 focus remains at the plasma membrane and is
539 gradually more distant from the nucleus due to oocyte enlargement (II.), before
540 disappearance. MEL-28::GFP signal is dimmer at times because the nucleus moves deeper in

541 the tissue (see also Movie S1). Asterisk marks the nucleus of the adjacent oocyte present
542 transiently in the vicinity.
543 **C.** Quantifications of RFP::SAS-7 focus movement velocity. Oocytes were between the -4 and
544 the -6 position at the beginning of the movies and imaged at least until the RFP::SAS-7 focus
545 reached the plasma membrane. Measurements were performed when the RFP::SAS-7 focus
546 moved mainly within the xy plane to ease quantification. Horizontal line: average speed. N=
547 7 oocytes.
548 **D, E.** Gonads from control worms (D) and *pcmd-1*(*t3412ts*) mutant animals at the restrictive
549 temperature (E), both expressing GFP::SAS-7 and RFP::SPD-5. Highlighted regions on the top
550 (1: early pachytene, EP; 2: rachis; 3: loop region) are shown magnified at the bottom as max
551 intensity projections of relevant z-slices , which can be different from those in the overview
552 image. Note absence of SPD-5 in *pcmd-1*(*t3412ts*) mutant animals as evidenced by the
553 presence of green foci. Note also that some nuclei lack centrioles already in early pachytene,
554 indicating that centrioles detach precociously, accumulating in the rachis and the loop region.
555 In the insets, dashed lines delineate the rachis and loop borders, dashed circles nuclei,
556 whereas arrowheads point to mislocalized centriolar foci.
557 **F-K.** Widefield images of gonads from worms of indicated RNAi conditions expressing
558 RFP::SAS-7 and RME-2::GFP (F, H, J) and corresponding quantifications (G, I, K). The presence
559 of centriolar foci was quantified (G, I, K: grey lines -SAS-7 total), distinguishing those at the
560 nuclear envelope (F, H, J: arrowheads) or detached from it (F,H,J: open arrowheads and G, I,
561 K: magenta dashed lines -SAS-7 detached). RME-2::GFP becomes progressively enriched at
562 the plasma membrane as the oocyte matures (see Fig.3B for confocal images). Note that
563 disappearance of centriolar foci occurs in a timely manner in all conditions as shown by SAS-
564 7 focus disappearance relative to oocyte maturation as quantified with RME-2::GFP increase.
565 In J, -5 oocyte, asterisk marks RFP::SAS-7 from a neighboring somatic cell. N: G=12; I=18; K=20.
566
567 **Figure 3. Depletion of PLKs does not lead to precocious centriole elimination**
568 **A.** Gonad expressing PLK-1::GFP and RFP::SAS-7. White squares highlight three regions
569 magnified as insets on the right. Arrowheads point to SAS-7 foci (magenta) and their
570 corresponding position in the PLK-1 channel (green). Asterisk marks PLK-1 on chromosomes.
571 Note that centriolar PLK-1 is present exclusively during mitosis (inset 1).

572 **B-K.** Gonads from worms of indicated genotypes and RNAi conditions expressing RME-2::GFP
573 and RFP::SAS-7 (B, D, F, H, J), together with corresponding quantifications (C, E, G, I, K) . Note
574 that in the double and triple mutant/RNAi conditions, RFP::SAS-7 decay and RME-2::GFP
575 enrichment at oocytes plasma membrane are shifted toward the loop but still occur in a
576 concomitant manner, approximately when 70% of oocytes contain both markers (horizontal
577 dashed line in the panels on the right). C : N=14 and R^2=0.96; E : N=12 and R^2=0.91; G : N=12
578 and R^2=0.87; I :N=18 and R^2=0.86; K=10 and R^2=0.81.
579
580 **Figure 4. Removal of the PCM core component SPD-5 does not impact centriole elimination**
581 **timing**
582 **A-C.** Gonads from worms of indicated genotypes expressing RFP::SPD-5 and GFP::SAS-7 (A, B)
583 and corresponding quantifications (C), illustrating persistence of SAS-7 foci despite absence
584 of SPD-5 in the *pcmd-1*(*t3421ts*) mutant at the restrictive temperature. Control: N=16;
585 *pcmd-1(t3421ts)*: N= 16.
586 **D.** Percentage of oocytes bearing SAS-7 foci and RME-2::GFP enriched at the plasma
587 membrane at indicated positions in control and *pcmd-1*(*t3421ts*) mutant worms at the
588 restrictive temperature. Control: N=15; *pcmd-1(t3421ts)*: N=13.
589
590 **Figure 5. Ultrastructural analysis reveals loss of central tube and centriole widening at**
591 **elimination onset**
592 **A.** Single focal plane brightfield image from a gonad expressing GFP::SAS-7 imaged after
593 chemical fixation and before resin embedding for electron-microscopy (EM) serial sectioning.
594 The gonad was straightened computationally for analysis purposes. Serially-sectioned nuclei
595 with centrioles are marked with filled white disks, those without centrioles with empty
596 squares. Orange numbers correspond to exemplary cases shown in E-H. Dashed orange line
597 marks the border between the syncytial region (to the top) and the cellularized region (to the
598 bottom). White rectangle corresponds to inset in B.
599 **B.** Magnified inset from A showing centriolar GFP::SAS-7 (left, arrowheads) relative to nuclei
600 (right, Brightfield (BF), dashed circles).
601 **C.** Corresponding 50nm EM section. Note alignment of nuclei between B and C (dashed
602 circles), which helps locating region corresponding to GFP::SAS-7 foci in the EM sections.

603 **D.** 50nm EM section of a pair of centrioles, one viewed from the top (top) and one from the
604 side (bottom), each with a procentriole (orange arrowheads).
605 **E-H. (i)** GFP::SAS-7 foci from the four positions numbered in orange in A. **(ii)** Corresponding
606 50nm EM sections of centrioles in top or tilted views, as indicated, illustrating stages of
607 elimination, with loss of central tube (F), of microtubule singlets (G), and of recognizable
608 centriolar ultrastructure (H). **(iii)** Overlay of EM images with indicated ultrastructural
609 compartments. **(iv)** Schematic representation of successive stages of elimination. The
610 electron dense material at the bottom right of images E(ii) and E(iii) is part of the endoplasmic
611 reticulum.
612 **I.** Centriole width and height, as well as diameter of indicated ultrastructural compartments,
613 at successive stages of centriole elimination, using distance from syncytium exit (dashed
614 orange line) as a proxy for time. Data acquired from 2 independent gonads (filled and empty
615 circles, respectively), using top, longitudinal and slightly tilted views for analysis (Materials
616 and methods). Numbered orange vertical lines indicate measurements made on centrioles
617 shown in E, F, G and H.
618 **J**. Color code and number of data points for each series in I, as well as r^2 values for trendlines
619 depicted as dashed lines. MT: microtubules.
620
621 **Figure 6. Centriole widening occurs concomitantly with the loss of the central tube protein**
622 **SAS-1 at the onset of centriole elimination**
623 **A.** Gonad immunostained with antibodies recognizing SAS-1::3xFLAG (green), SAS-4
624 (magenta) and GFP::SAS-7 (cyan); DNA counterstain: grey. Seven sub-regions within early
625 prophase, late pachytene and diplotene regions were defined as indicated. Each region is
626 approximately three times the diameter of a diplotene nucleus. White squares correspond to
627 insets in B.
628 **B.** Magnified insets from A, illustrating earlier loss of centriolar SAS-1 compared to SAS-7 and
629 SAS-4 (arrowheads).
630 **C.** Normalized fluorescence intensity for SAS-1, SAS-7 and SAS-4 across the seven sub-regions
631 illustrated in panel A. The background-subtracted signal of foci was averaged for each region
632 and normalized to the mean value in region 1. Mean ± SD for each region; N= 7 gonads.
633 **D-F.** U-Ex-STED of centrioles at indicated stages (early prophase, late pachytene and
634 diplotene) from worms expressing GBP::RFP::SAS-1 (D), SPD-2::GFP (E) and SAS-4 (F), stained

635 for RFP or GFP and co-stained with an antibody against α-tubulin. The LUT "Fire" reports
636 fluorescence intensity (from bright to dim: white, yellow, red, purple, blue and black). The
637 expansion factor is the same for each sample so that relative sizes within each series can be
638 compared (i.e. within D, E and F). Note that we used GBP::RFP::SAS-1 instead of SAS-1::3xFLAG
639 in these experiments as RFP antibodies gave stronger signals than FLAG antibodies, allowing
640 better detection following U-Ex-STED. D, grey boxes were used because of the impossibility
641 to identify centrioles remnant based on the tubulin staining at the oocytes stage.
642 **G.** Normalized fluorescence intensity of GBP::RFP::SAS-1, SPD-2::GFP and SAS-4 during
643 prophase progression determined from U-Ex-STED images. All values were background-
644 subtracted and first normalized to the α-tubulin signal intensity in the same centriole and
645 then to the mean value of early prophase within each series. N (early prophase, late
646 pachytene, diplotene): GBP::RFP::SAS-1/α-tubulin: 15, 14, 16; SPD-2::GFP/α-tubulin: 42, 26,
647 41; SAS-4/α-tubulin: 22, 10, 15. In box-plots in this and other figures, the middle line
648 corresponds to the median and the cross to the mean; boxes include 50% of values (IQR) and
649 whiskers show the range of values within 1.5*IQR.
650 **H.** Relative diameter during prophase progression of rings formed by the three indicated
651 proteins from centriole top views imaged by U-Ex-STED. For each series, values were
652 normalized to the mean diameter at diplotene. N (early prophase, late pachytene, diplotene):
653 SPD-2: 34, 26, 31; SAS-4: 22, 10, 18; α-tubulin: 17, 10, 16.
654
655 **Figure 7. SAS-1 is required for proper centriole integrity during oogenesis**
656 **A, B.** U-Ex-STED top views of centrioles during prophase progression from control (A) and
657 *sas-1(t1521ts)* mutant at the restrictive temperature (B) stained for α-tubulin (magenta) and
658 SAS-4 (green).
659 **C.** Corresponding SAS-4 relative ring diameter from top views imaged by U-Ex-STED. For each
660 series, values were normalized by the mean diameter at diplotene. N (early prophase,
661 diplotene): control: 21, 18; *sas-1(t1521ts)*: 22, 13.
662 **D.** U-Ex-STED top views of early prophase centrioles from control (left) and *sas-1(t1521ts)*
663 mutant (right), together with corresponding brightness distributions of the 9 discrete SAS-4
664 signals (center). Each vertical column displays the 9 signals measured in one centriole

665 normalized to the mean signal intensity of that centriole. The two distributions are statistically
666 different (Levene test, p-value<0.00001).
667 **E, F.** Evolution of normalized α-tubulin (E) and SAS-4 (F) fluorescence intensity during
668 prophase progression in samples imaged by U-Ex-STED. Values were background-subtracted
669 and normalized to the mean of early prophase measurements in each series. N (prophase,
670 late pachytene, diplotene): control: 17, 10, 16; *sas-1(t1521ts)*: 24, 32, 20.
671 **G.** Number of discrete SAS-4 foci in centrioles in early prophase and diplotene nuclei of
672 control and *sas-1(t1521ts)* mutant, together with exemplary U-Ex-STED images. N (early
673 prophase, diplotene): control: 27, 14; *sas-1(t1521ts)*: 25, 18.
674

675 ## Materials and methods

676 ### *C. elegans* strains and RNAi

677 The *C. elegans* lines generated for this study (see Table1) are available from the lead contact
678 upon request. Strains were maintained following standard methods on nematode growth
679 medium (NGM) plates seeded with *Escherichia coli* OP50 as food source (Brenner, 1974).
680 Strains were kept at 20°C or 24°C, except for thermosensitive strains, which were kept at 16°C
681 until the L4 stage, when they were shifted to 24°C or 25°C for 20-24 h prior to imaging. The
682 list of strains used in this study is given in Table S1. Synchronized populations were obtained
683 by allowing 20-50 gravid adults to lay eggs for 1 h at room temperature (RT) and imaging
684 gonads of the resulting adults after ~65h of growth at 20°C. RNAi by feeding was performed
685 with clones from either Ahringer or Vidal library to deplete *plk-1*(Vidal), *tba-2* (Vidal), *dhc-1*
686 (Arhinger), *dlc-1* (Vidal), *act-1* (Vidal) and *unc-116* (Arhinger), feeding L3/young L4s at 24°C
687 and imaging 20-24h thereafter.
688

689 ### Gonad spreading

690 Spreading of *C. elegans* gonads was performed similarly as in (Woglar et al., 2022). Gonads of
691 ~ 1000 adult worms were dissected in 30 µL PBS-T (0.2 x PBS, 1:1000 Tween 20) on an ethanol-
692 washed 22x40 mm coverslip. 5-10 µL of dissected gonads were then pipetted onto a new
693 ethanol-washed 22x40 mm coverslip and 50 µL of spreading solution (for one coverslip, 50
694 µL: 32 µL of Fixative was added (4% w/v Paraformaldehyde and 3.2% w/v Sucrose in water),
695 16 µL of Lipsol solution (1% v/v/ Lipsol in water), 2 µL of Sarcosyl solution (1% w/v of Sarcosyl
696 in water), and gonads were immediately distributed over the coverslip using a pipette tip.

697 Coverslips were left to dry at room temperature (RT) followed by incubation at 37˚C for 1h.
698 Coverslips were either processed for staining and expansion or stored at -80˚C.
699
700 **Gonads expansion for U-Ex-STED**
701 Ultrastructure expansion microscopy was performed as in (Woglar et al., 2022). In brief, dried
702 coverslips were incubated for 20 min in methanol at −20˚C and washed 3 times in PBS-T for 5
703 min, followed by two 5 min washes in PBS. Coverslips were incubated with mild agitation in a
704 5cm Petri dish overnight at RT in Acrylamide/Formaldehyde solution (1% Acrylamide and 1%
705 Formaldehyde in PBS). Thereafter, coverslips were washed 3 times 5 min in PBS. For gelation,
706 coverslips were incubated in 50 µl monomer solution (19% (wt/wt) Sodium Acrylate, 10%
707 (wt/wt) Acrylamide, 0.05% (wt/wt) BIS in PBS) supplemented with 0.5%
708 Tetramethylethylenediamine (TEMED) and 0.5% Amonium Persulfate (APS) on a piece of
709 Parafilm for 1h at 37˚C in a moist chamber in the dark. All subsequent steps were carried out
710 under mild agitation at room temperature unless otherwise stated. Gels were incubated in
711 5cm Petri dishes for 15 min in denaturation buffer (200 mM SDS, 200 mM NaCl and 50 mM
712 Tris in distilled water, pH=9) followed by incubation for 1 h on a 95˚C hot plate in fresh
713 denaturation buffer. Gels were transferred to 15 cm Petri dishes, washed with distilled water
714 5 times for 20 min, followed by incubation in distilled water overnight at 4˚C. The expansion
715 factor was estimated by measuring the gel size with a ruler.
716
717 **Immunostainings on whole dissected gonads and expanded germ cell nuclei**
718 Gonads were dissected in sperm buffer (50 mM Hepes (pH 7.0), 50 mM NACL, 25 mM KCL, 5
719 mM CaCl2, 1 mM MgSO4, 50 mM Glucose, 1 mg/ml BSA), transferred onto slides (Marienfeld,
720 1000200) coated with poly-lysine (2 mg/ml in PBS), freeze-cracked and fixed in cold methanol
721 for 5 min. Slides were then incubated overnight at RT in blocking buffer (3% BSA in PBST) with
722 primary antibodies as follows: mouse anti-IFA-1 (1:100, ATCC-TIB-131 (Pruss et al., 1981));
723 chicken-anti-GFP (1:500, Abcam ab13970), rabbit-anti-SAS-4 (1:800 (Leidel and Gönczy,
724 2003)); mouse-anti-Flag (1:200, Sigma-Aldrich F1804). Slides were then washed twice 10 min
725 in PBS-T, incubated with anti-chicken Alexa Fluor 488 (1:1000, A11039), anti-rabbit Alexa
726 Fluor 647 (1:1000, A10523), anti-mouse Alexa Fluor 568 (1:1000, A11004) in PBS-T for 2h at
727 RT, washed three times 10min in PBS-T, counterstained with Hoechst (1:1000) and mounted
728 in mounting medium (4% n-Propyl-Gallate, 90% Glycerol, 1xPBS).

729 After expansion, gels were cut into pieces fitting into a 5 cm Petri dish. Prior to staining, gels
730 were blocked for 1h at RT in blocking buffer (10mM HEPES (pH=7.4), 3% BSA, 0.1% Tween 20,
731 sodium azide (0.05%)), followed by incubation overnight at RT with primary antibodies diluted
732 in blocking buffer. Gels were washed three times in blocking buffer for 10 min each, before
733 incubation with secondary antibodies diluted in blocking buffer supplemented with 0.7 ug/L
734 Hoechst for 3 h at 37˚C in the dark. Gels were washed three times in blocking buffer for 10
735 min each before transfer into a 10cm Petri dish for re-expansion by washing 6 times 20 min
736 in distilled water. For imaging, gels were cut and mounted on a 60x24 mm coverslip coated
737 with poly-D-lysine (Sigma, # P1024) diluted in water (2 mg/ml) and supported on both
738 longitudinal sides with capillaries attached with superglue. To prevent drying, the edges of
739 the gel were covered with VaLaP (1:1:1 petroleum:jelly:lanolin:paraffin wax), and the gel
740 covered with Halocarbon oil 700 for imaging. Antibodies used on expanded gels were as
741 follows: rabbit anti-SAS-6 (1:1000 (Leidel et al., 2005)), rabbit anti-SAS-4 (1:800 (Leidel and
742 Gönczy, 2003)), rabbit anti-SAS-5 (1 :50 (Delattre et al., 2004)), rabbit anti-GFP (1:250, a gift
743 from Viesturs Simanis), mouse anti-RFP(RF5R) (1:500, Thermo Fisher, MA5-15257), rabbit
744 anti-α-tubulin (1:500, Abcam (ab52866)) and rat anti-tyrosine α-tubulin (1:500, EMD
745 Millipore, MAB1864). Secondary antibodies (all used at 1:1000) were as follows: donkey anti-
746 rabbit conjugated to Alexa Fluor 594 (Abcam, ab150072), goat anti-rat conjugated to Alexa
747 Fluor 594 (Thermo Fisher, A11007), goat anti-rabbit conjugated to Alexa Fluor 488 (Thermo
748 Fisher, A11034) and donkey anti-rat conjugated to Alexa Fluor 488 (Invitrogen, A21208).
749
750 **Microscopy**
751 For live gonad imaging, worms were mounted on 2% agarose pads and immobilized with 8 μl
752 of 100mM sodium azide (NaN_3). Spinning disc confocal imaging was performed using an
753 inverted Olympus IX 83 motorized microscope equipped with a Yokogawa spinning disk
754 CSU-W1 head, a 60× (NA 1.42 U PLAN S APO) objective, an ImagEMX2 EMCCD and an Orca
755 Flash 4.0 sCMOS camera, controlled by VisiView software. Widefield imaging was performed
756 using an inverted Nikon eclipse Ti2-U widefield microscope, with a Nikon Plan Apo 60x/1.40
757 ∞/0.17 WD 0.13 objective. The microscope was equipped with a Nano Z500 super long-range
758 Piezo z-stage, a Märzhäuser Tango 3 desktop controller together with the Ergodrive 3 3-axes
759 operating device, a Lumencor Spectra4 as light source, an Andor Zyla-4.2P CL10 sCMOS
760 camera, and was controlled by Micromanager (Edelstein et al., 2014). For time-lapse imaging,

761 worms were partially immobilized in a microfluidic device enabling continuous feeding
762 (Berger et al., 2018). For U-Ex-STED, stages of meiotic prophase were identified by chromatin
763 morphology visualized with Hoechst (Phillips et al., 2009). 2D-STED images were acquired on
764 a Leica TCS SP8 STED 3X microscope with a 100 x 1.4 NA oil-immersion objective, using 488
765 nm and 589 nm excitation, and 592 nm and 775 nm pulsed lasers for depletion. 1-pixel
766 Gaussian blur was applied to all images for analysis and display. For display, brightness and
767 contrast was adjusted in the individual channels using Fiji, keeping the same settings within a
768 series.
769
770 **Image processing and analysis**
771 Microscopy images were stitched, rotated, z-projected; gray levels were then adjusted using
772 Fiji (ImageJ). Gonad images and insets are maximum intensity projection of relevant planes.
773 For dual color quantifications of live imaging at the spinning disc confocal, a ROI of 15x15
774 pixels was centered on each focus at the z-slice displaying the maximum brightness; Max
775 intensity projection of 12 μm around this position was applied to generate a 2D image.
776 Projection on one of the axes then provided a 1D intensity profile. We fitted the function
777 y=a+b*x+c*exp(-/x-d)*(x-d)/e) on this profile and subtracted linear background through the
778 first and the last data point. The integration over the resulting curve gave the reported
779 intensity value for one focus. Values for foci in oocytes from different gonads located at the
780 same position with respect to the spermatheca were averaged. Fluorescence intensity curves
781 were normalized according to the maximal and minimal values of all oocytes for each marker.
782 ImageJ macro used for quantifications is on GitHub
783 (https://github.com/UPGON/pierron2023-centriole-elimination). In the case of
784 RME-2::GFP, an oocyte was scored as positive when the four sides of the plasma membrane
785 exhibited GFP fluorescence. For quantification of immunostaining in Fig. 6C, sum-projected
786 images of gonads were divided into seven regions separated approximately by three times
787 the diameter of diplotene nuclei at the beginning of cellularization. ROIs of 0.5-2 μm^2 were
788 drawn around each focus, as well as just next to it for background subtraction. The
789 background-corrected signal was then determined for each channel, and the average signal
790 for each region normalized with that of the most-distal region 1.
791 **Timelapse imaging and movie analysis**

792 For long-term live imaging, worms were loaded and immobilized in the microfluidic as
793 described (Berger et al., 2018). Briefly, synchronized day 1 adults were collected and washed
794 3 times in fresh S-basal buffer (5.85 g NaCl, 1 g K_2HPO_4, 6 g KH_2PO, 1 ml cholesterol (5 mg/ml
795 in ethanol), H_2O to 1L) and left to sediment. In parallel, a 50 ml Falcon tube of NA22 grown
796 overnight at 37°C was centrifuged (at 4000rcf for 20 min) to obtain a bacteria pellet. This
797 pellet was washed 3 times in S-basal and resuspended in 1 ml S-basal supplemented with
798 0.65mL of Optiprep (density matching to prevent bacteria from segregating, 1114542 by
799 Serumwerk Bernburg for Alere Technologies) and 0.332 mL of S-Basal+1% Pluronic F127
800 (P2443, Sigma-Aldrich). This food mixture was filtered through a 10µm cell strainer (#43-
801 10010-50, pluriSelect) to remove bacteria clumps. The microfluidic device was set up on the
802 Nikon eclipse Ti2-U widefield microscope. The food supply was connected to the device, and
803 the worms were loaded and immobilized for imaging. Worms were positioned so that the
804 proximal part of the posterior gonad was always closest to the coverslip. Movies were
805 acquired during of 3-5 h with 2min intervals and binning 2. We filmed 13 worms among which
806 2 were excluded because of apparent signs of starvation. Among the 11 worms analyzed, 6
807 are expressing MEL-28::GFP and 5 are expressing RME-2::GFP, together with RFP::SAS-7.
808 We focused on oocytes in positions -6 to -4 at the onset of the experiment, so that the entire
809 movement of foci could be monitored. Cropped images were extracted and aligned based on
810 the center of the nucleus, which was manually selected at each timepoint for a given oocyte.
811 using. For 7 movies, kymographs were generated using a line width of 40 and the
812 KymographBuilder plugin in Fiji (Mary et al., 2016). Centriolar foci remnant speed was
813 calculated using the maximum distance between the green signal and the magenta signal on
814 the Kymograph during the centriolar focus migration phase. The graph was generated using
815 PlotsofData (Postma and Goedhart, 2019).
816
817 **CLEM analysis**
818 Gonads of genotype *sas-7(or1940[gfp::sas-7])III; glo-1(zu931)X; itIs37[pie-1p::mCherry::H2B,*
819 *unc-119(+)]* or *ltSi202[pVV103/ pOD1021; Pspd-2::GFP::SPD-5 RNAiresistant;cb-unc-119(+)]II;*
820 *sas-7(is1[tagRFP::sas-7+loxP])III; glo-1(zu931)X* were dissected in sperm buffer and
821 transferred onto poly-lysine-coated MatTek glass bottom dishes. 3D imaging of gonads was
822 performed using the previously mentioned Nikon widefield microscope set up, before and
823 after an approximately 2h30 min fixation at RT in 2.2% glutaraldehyde, 0.9%

824 Paraformaldehyde in Cacodylate buffer 0.05M (pH7.4), 0.09M sucrose, and 0.9mM MgCl2.
825 Briefly, specimens were postfixed in 1% osmium tetroxide, 0.8% potassium ferrocyanide in
826 cacodylate buffer (0.1 M, pH 7.2), treated with 0.2% Tannic Acid in 0.05M cocadylate buffer
827 (pH 7.0), stained with 1% uranyl acetate in Sodium Acetate (pH 5.2), dehydrated in an alcohol
828 series, and embedded in Hard EPON. 50-nm sections were imaged at 23,000x magnification
829 using a TecnaiSpirit (FEI) operated at 80 kV and equipped with an Eagle CCD camera (FEI).
830 Using the relative position of GFP::SAS-7 foci and neighboring nuclei in fluorescence images
831 facilitated the search for centrioles in EM serial sections. Gray values were adjusted and
832 Gaussian blur filtering 1.5 was applied on the displayed EM images. The two gonads analyzed
833 were straightened using the "Straighten" Fiji plugin (KOCSIS et al., 1991) and the distance of
834 each nucleus studied to the syncytium exit was determined. For measurements of
835 ultrastructural elements, each data point is the average of 4 measurements extracted from
836 lines drawn along the height of the feature. In some cases, ultrastructural elements could not
837 be measured because they were not visualized accurately, the view of the centriole was too
838 tilted or it was not apparent anymore due to ongoing elimination.
839
840 **Quantification and statistical analysis**
841 For Fig.1 and Fig.2, correlation between the 2 markers for each condition was determined
842 taking into account the 12 or 15 positions respectively. R^2 of fits are mentioned in the legends.
843 Levene's test for equality or inequality of variance was performed by using:
844 https://www.socscistatistics.com/tests/levene/default.aspx. Required normality of input
845 data was tested for and confirmed to be not significantly different from normal distribution
846 by performing a Kolmogorov-Smirnov test (p-value for WT: 0.797 and *sas-1(ts)*: 0.993) using:
847 https://www.socscistatistics.com/tests/kolmogorov/default.aspx
848
849 **Table 1: list of strains used in this study**

Strain name	Genotype	Origin
GZ1416	*sas-7(or1940(gfp::sas-7))III; glo-1(zu931)X; ltIs64 [pOD333; pie-1/mCherry-tev-Stag::sas-4 genomic; unc-119 (+) genomic}*	(Dammermann et al., 2008; Sugioka et al., 2017) and this study

GZ1502	*spd-2(vie4[spd-2::gfp +loxP]) I; sas-7(is1[tagRFP::sas-7+loxP])III; glo-1(zu931)X*	(Garbrecht et al., 2021; Klinkert et al., 2019) and this study
GZ1501	*ItSi40{pOD1227:psas-6::sas-6reencoded::GFP;Cb-unc-119(+)}II; sas-7(is1[tagRFP::sas-7+loxP])III; glo-1(zu931)X*	(Klinkert et al., 2019; Qiao et al., 2012) and this study
GZ1946	*spd-5(wow36[tagrfp-t^3xmyc::spd-5])I; sas-7(or1940[gfp::sas-7])III*	(Klinkert et al., 2019; Magescas et al., 2019) and this study
GZ1297	*unc-119(ed3) III; ltIs68 [pOD348; pie-1/gfp-tev-Stag::hyls-1 cDNA; unc-119 (+) genomic*	OD94 (Dammermann et al., 2009)
GZ1721	*gip-1(wow3[GFP:GIP-1]) sas-7(is1[tagRFP::sas-7+loxP])III; glo-1(zu931)X*	(Sallee et al., 2018) and this study
GZ1944	*pcmd-1(syb486[gfp::pcmd-1]) I; sas-7(is1[tagRFP::sas-7+loxP])III*	TMD119 (Erpf et al., 2019) and this study
GZ1688	*mzt-1(wow51[GFP:MZT-1])I; sas-7(is1[tagRFP::sas-7+loxP])III; glo-1(zu931)X*	(Sallee et al., 2018) and this study
GZ1727	*zif-1(gk117) sas-7(is3[tagRFP::sas-7+loxP])III; air-1(wow14[AIR-1:ZF:GFP])V*	(Sallee et al., 2018) and this study
GZ1760	*zyg-9(wow13[ZYG-9:ZF:GFP]II; zif-1(gk117) sas-7(is3[tagRFP::sas-7+loxP])III*	(Sallee et al., 2018) and this study
GZ1633	*mel-28(bq5[GFP::mel-28])III sas-7(Is1 RFPSAS-7KI)III*	(Gómez-Saldivar et al., 2016) and this study
GZ1947	*spd-5(wow36[tagrfp-t^3xmyc::spd-5]) pcmd-1(t3421)I; sas-7(or1940[gfp::sas-7])III*	(Erpf et al., 2019) and TMD237, made by Mikeladze-Dvali T.
GZ1838	*sas-7(is1[tagRFP::sas-7+loxP])III; pwIs116[rme-2p::rme-2::GFP::rme-2 3'UTR + unc-119(+)]*	(Balklava et al., 2007; Klinkert et al., 2019) and this study
GZ1807	*sas-7(is1[tagRFP::sas-7+loxP])III; fem-1ts(hc17)IV; pwIs116[rme-2p::rme-2::GFP::rme-2 3'UTR + unc-119(+)]*	(Nelson et al., 1978) and this study

GZ1761	*plk-1(lt17[plk-1::sgfp+loxP]) sas-7(is4[tagRFP::sas-7+loxP])III*	(Han et al., 2018) and this study
GZ1762	*plk-2(ok1936)II; sas-7(is1[tagRFP::sas-7+loxP])III; pwIs116[rme-2p::rme-2::GFP::rme-2 3'UTR + unc-119(+)]*	(Harper et al., 2011) and this study
GZ1600	*plk-2(ok1936) I; sas-7(is1[tagRFP::sas-7+loxP])III; plk-3(gk1103) IV; pwIs116[rme-2p::rme-2::GFP::rme-2 3'UTR + unc-119(+)]*	This study
GZ1864	*spd-2(is2[tagRFP::spd-2 +loxP]) spd-5(vie26[gfp::spd-5 +loxP])I; pwIs116[rme-2p::rme-2::GFP::rme-2 3'UTR + unc-119(+)]*	(Klinkert et al., 2019) and this study
GZ1865	*plk-2(ok1936) spd-2(is2[tagRFP::spd-2 +loxP]) spd-5(vie26[gfp::spd-5 +loxP])I/hT2[qIs48] I; plk-1(or683ts)/hT2 III; pwIs116[rme-2p::rme-2::GFP::rme-2 3'UTR + unc-119(+)]*	(Harper et al., 2011; Klinkert et al., 2019; O'Rourke et al., 2011) and this study.
GZ1786	*plk-2(ok1936)/hT2[qIs48] I; plk-1(or683ts)/hT2 III ; him-6(jf93[him-6::HA] IV*	A gift from A. M. Villeneuve
GZ1738	*sas-7(is1[tagRFP::sas-7+loxP])III; glo-1(zu931)X; pwIs116[rme-2p::rme-2::GFP::rme-2 3'UTR + unc-119(+)]*	This study
GZ1948	*pcmd-1(t3421) / hT2 I; sas-7(is1[rfp::sas-7+loxP]) III; glo-1(zu931) X ; pwIs116[rme-2p::rme-2::GFP::rme-2 3'UTR + unc-119(+)]*	TMD140, made by Mikeladze-Dvali T.
GZ1414	*sas-7(or1940[gfp::sas-7])III; glo-1(zu931)X; itIs37[pie-1p::mCherry::H2B, unc-119(+)]*	(Sugioka et al., 2017) and this study
GZ1712	*ltSi202[pVV103/ pOD1021; Pspd-2::GFP::SPD-5 RNAiresistant;cb-unc-119(+)]II; sas-7(is1[tagRFP::sas-7+loxP])III; glo-1(zu931)X*	(Wueseke et al., 2016) and this study
GZ1986	*sas-7(or1940[gfp::sas-7]) sas-1(is6[sas-1::3xflag])III*	(Sugioka et al., 2017) and this study
GZ1965	*isSi9[Pmex-5::GBP::tagRFP-T::sas-1::tbb-2 3'UTR cb-unc-119(+)] II; unc-119(ed3)III.*	This study
GZ1990	*spd-2(vie4[spd-2::gfp +loxP])I; sas-7(is1[tagRFP::sas-7+loxP])III sas-1(t1521)/hT2*	(von Tobel et al., 2014) and this study

850

851 **Movie S1. Centriolar focus movement from the nuclear envelope to the plasma membrane**

852 Widefield time lapse imaging of an oocyte from a worm immobilized in the microfluidic device
853 and expressing MEL-28::GFP as well as RFP::SAS-7. Top: brightfield; bottom: max projection
854 of relevant optical slides of the merge between MEL-28::GFP (green) and RFP::SAS-7

855 (magenta). Note that the RFP::SAS-7 centriolar focus detaches from the nuclear envelope at
856 0 min, then migrates to the plasma membrane, which is reached at 52 min, before the foci
857 becoming undetectable at 166 min.
858
859

860 **REFERENCES**

861 Adam Bohnert, K., Kenyon, C., 2017. A lysosomal switch triggers proteostasis renewal in the
862 immortal C. Elegans germ lineage. Nature 551, 629–633.
863 https://doi.org/10.1038/nature24620
864 Balestra, F.R., Domínguez-Calvo, A., Wolf, B., Busso, C., Buff, A., Averink, T., Lipsanen-
865 Nyman, M., Huertas, P., Ríos, R.M., Gönczy, P., 2021. TRIM37 prevents formation of
866 centriolar protein assemblies by regulating Centrobin. Elife 10, 1–76.
867 https://doi.org/10.7554/eLife.62640
868 Balklava, Z., Pant, S., Fares, H., Grant, B.D., 2007. Genome-wide analysis identifies a general
869 requirement for polarity proteins in endocytic traffic. Nat. Cell Biol. 9, 1066–1073.
870 https://doi.org/10.1038/ncb1627
871 Banterle, N., Gönczy, P., 2017. Centriole Biogenesis: From Identifying the Characters to
872 Understanding the Plot. Annu. Rev. Cell Dev. Biol. 33, 23–49.
873 https://doi.org/10.1146/annurev-cellbio-100616-060454
874 Berger, S., Lattmann, E., Aegerter-Wilmsen, T., Hengartner, M., Hajnal, A., DeMello, A.,
875 Casadevall i Solvas, X., 2018. Long-term C. elegans immobilization enables high
876 resolution developmental studies in vivo. Lab Chip 18, 1359–1368.
877 https://doi.org/10.1039/C7LC01185G
878 Bornens, M., 2012. The Centrosome in Cells and Organisms. Science (80-.). 335, 422–426.
879 https://doi.org/10.1126/science.1209037
880 Borrego-Pinto, J., Somogyi, K., Karreman, M.A., König, J., Müller-Reichert, T., Bettencourt-
881 Dias, M., Gönczy, P., Schwab, Y., Lénárt, P., 2016. Distinct mechanisms eliminate
882 mother and daughter centrioles in meiosis of starfish oocytes. J. Cell Biol. 212, 815–
883 827. https://doi.org/10.1083/jcb.201510083
884 Brandt, J.N., Kim, Y., 2021. Targeting Polo-like kinase in space and time during C. elegans
885 meiosis. Cell Cycle 20, 1519–1526. https://doi.org/10.1080/15384101.2021.1953232
886 Brenner, S., 1974. The genetics of Caenorhabditis elegans. Genetics 77, 71–94.
887 Budirahardja, Y., Gönczy, P., 2008. PLK-1 asymmetry contributes to asynchronous cell
888 division of C. elegans embryos. Development 135, 1303–1313.
889 https://doi.org/10.1242/dev.019075
890 Chang, T.-J.B., Hsu, J.C.C., Yang, T., 2023. Single-molecule localization microscopy of
891 expanded mammalian centrioles unravels the ultrastructural constitution of distal

892 appendages. Biophys. J. 122, 17a. https://doi.org/10.1016/j.bpj.2022.11.317
893 Chase, D., Serafinas, C., Ashcroft, N., Kosinski, M., Longo, D., Ferris, D.K., Golden, A., 2000.
894 The polo-like kinase PLK-1 is required for nuclear envelope breakdown and the
895 completion of meiosis inCaenorhabditis elegans. genesis 26, 26–41.
896 https://doi.org/10.1002/(SICI)1526-968X(200001)26:1<26::AID-GENE6>3.0.CO;2-O
897 Crosio, C., Fimia, G.M., Loury, R., Kimura, M., Okano, Y., Zhou, H., Sen, S., Allis, C.D.,
898 Sassone-Corsi, P., 2002. Mitotic Phosphorylation of Histone H3: Spatio-Temporal
899 Regulation by Mammalian Aurora Kinases. Mol. Cell. Biol. 22, 874–885.
900 https://doi.org/10.1128/MCB.22.3.874-885.2002
901 Crowder, M.E., Strzelecka, M., Wilbur, J.D., Good, M.C., von Dassow, G., Heald, R., 2015. A
902 comparative analysis of spindle morphometrics across metazoans. Curr. Biol. 25, 1542–
903 50. https://doi.org/10.1016/j.cub.2015.04.036
904 Dammermann, A., Maddox, P.S., Desai, A., Oegema, K., 2008. SAS-4 is recruited to a
905 dynamic structure in newly forming centrioles that is stabilized by the γ-tubulin–
906 mediated addition of centriolar microtubules. J. Cell Biol. 180, 771–785.
907 https://doi.org/10.1083/jcb.200709102
908 Dammermann, A., Pemble, H., Mitchell, B.J., McLeod, I., Yates, J.R., Kintner, C., Desai, A.B.,
909 Oegema, K., 2009. The hydrolethalus syndrome protein HYLS-1 links core centriole
910 structure to cilia formation. Genes Dev. 23, 2046–2059.
911 https://doi.org/10.1101/gad.1810409
912 Delattre, M., Gönczy, P., 2004. The arithmetic of centrosome biogenesis. J. Cell Sci. 117,
913 1619–1630. https://doi.org/10.1242/jcs.01128
914 Delattre, M., Leidel, S., Wani, K., Baumer, K., Bamat, J., Schnabel, H., Feichtinger, R.,
915 Schnabel, R., Gönczy, P., 2004. Centriolar SAS-5 is required for centrosome duplication
916 in C. elegans. Nat. Cell Biol. 6, 656–664. https://doi.org/10.1038/ncb1146
917 Doroquez, D.B., Berciu, C., Anderson, J.R., Sengupta, P., Nicastro, D., 2014. A high-resolution
918 morphological and ultrastructural map of anterior sensory cilia and glia in
919 Caenorhabditis elegans. Elife 2014, 1–35. https://doi.org/10.7554/eLife.01948
920 Edelstein, A.D., Tsuchida, M.A., Amodaj, N., Pinkard, H., Vale, R.D., Stuurman, N., 2014.
921 Advanced methods of microscope control using μManager software. J. Biol. Methods 1,
922 e10. https://doi.org/10.14440/jbm.2014.36
923 Erpf, A.C., Stenzel, L., Memar, N., Antoniolli, M., Osepashvili, M., Schnabel, R., Conradt, B.,

924 Mikeladze-Dvali, T., 2019. PCMD-1 Organizes Centrosome Matrix Assembly in C.
925 elegans. Curr. Biol. 29, 1324-1336.e6. https://doi.org/10.1016/j.cub.2019.03.029
926 Galy, V., Askjaer, P., Franz, C., López-Iglesias, C., Mattaj, I.W., 2006. MEL-28, a Novel
927 Nuclear-Envelope and Kinetochore Protein Essential for Zygotic Nuclear-Envelope
928 Assembly in C. elegans. Curr. Biol. 16, 1748–1756.
929 https://doi.org/10.1016/j.cub.2006.06.067
930 Garbrecht, J., Laos, T., Holzer, E., Dillinger, M., Dammermann, A., 2021. An acentriolar
931 centrosome at the C. elegans ciliary base. Curr. Biol. 31, 2418-2428.e8.
932 https://doi.org/10.1016/j.cub.2021.03.023
933 Gaudin, N., Martin Gil, P., Boumendjel, M., Ershov, D., Pioche-Durieu, C., Bouix, M.,
934 Delobelle, Q., Maniscalco, L., Phan, T.B.N., Heyer, V., Reina-San-Martin, B., Azimzadeh,
935 J., 2022. Evolutionary conservation of centriole rotational asymmetry in the human
936 centrosome. Elife 11, 1–24. https://doi.org/10.7554/eLife.72382
937 Giet, R., McLean, D., Descamps, S., Lee, M.J., Raff, J.W., Prigent, C., Glover, D.M., 2002.
938 Drosophila Aurora A kinase is required to localize D-TACC to centrosomes and to
939 regulate astral microtubules. J. Cell Biol. 156, 437–451.
940 https://doi.org/10.1083/jcb.200108135
941 Gomes Pereira, S., Dias Louro, M.A., Bettencourt-Dias, M., 2021. Biophysical and
942 Quantitative Principles of Centrosome Biogenesis and Structure. Annu. Rev. Cell Dev.
943 Biol. 37, 43–63. https://doi.org/10.1146/annurev-cellbio-120219-051400
944 Gómez-Saldivar, G., Fernandez, A., Hirano, Y., Mauro, M., Lai, A., Ayuso, C., Haraguchi, T.,
945 Hiraoka, Y., Piano, F., Askjaer, P., 2016. Identification of Conserved MEL-28/ELYS
946 Domains with Essential Roles in Nuclear Assembly and Chromosome Segregation. PLOS
947 Genet. 12, e1006131. https://doi.org/10.1371/journal.pgen.1006131
948 Gönczy, P., Pichler, S., Kirkham, M., Hyman, A.A., 1999. Cytoplasmic dynein is required for
949 distinct aspects of MTOC positioning, including centrosome separation, in the one cell
950 stage Caenorhabditis elegans embryo. J. Cell Biol. 147, 135–150.
951 https://doi.org/10.1083/jcb.147.1.135
952 Grant, B., Hirsh, D., 1999. Receptor-mediated endocytosis in the Caenorhabditis elegans
953 oocyte. Mol. Biol. Cell 10, 4311–4326. https://doi.org/10.1091/mbc.10.12.4311
954 Hamill, D.R., Severson, A.F., Carter, J.C., Bowerman, B., 2002. Centrosome Maturation and
955 Mitotic Spindle Assembly in C. elegans Require SPD-5, a Protein with Multiple Coiled-

956 Coil Domains. Dev. Cell 3, 673–684. https://doi.org/10.1016/S1534-5807(02)00327-1
957 Han, B., Antkowiak, K.R., Fan, X., Rutigliano, M., Ryder, S.P., Griffin, E.E., 2018. Polo-like
958 Kinase Couples Cytoplasmic Protein Gradients in the C. elegans Zygote. Curr. Biol. 28,
959 60-69.e8. https://doi.org/10.1016/j.cub.2017.11.048
960 Harper, N.C., Rillo, R., Jover-Gil, S., Assaf, Z.J., Bhalla, N., Dernburg, A.F., 2011. Pairing
961 Centers Recruit a Polo-like Kinase to Orchestrate Meiotic Chromosome Dynamics in C.
962 elegans. Dev. Cell 21, 934–947. https://doi.org/10.1016/j.devcel.2011.09.001
963 Jaramillo-Lambert, A., Ellefson, M., Villeneuve, A.M., Engebrecht, J., 2007. Differential timing
964 of S phases, X chromosome replication, and meiotic prophase in the C. elegans germ
965 line. Dev. Biol. 308, 206–221. https://doi.org/10.1016/j.ydbio.2007.05.019
966 Klinkert, K., Levernier, N., Gross, P., Gentili, C., von Tobel, L., Pierron, M., Busso, C.,
967 Herrman, S., Grill, S.W., Kruse, K., Gönczy, P., 2019. Aurora A depletion reveals
968 centrosome-independent polarization mechanism in Caenorhabditis elegans. Elife 8, 1–
969 31. https://doi.org/10.7554/eLife.44552
970 KOCSIS, E., TRUS, B., STEER, C., BISHER, M., STEVEN, A., 1991. Image averaging of flexible
971 fibrous macromolecules: The clathrin triskelion has an elastic proximal segment. J.
972 Struct. Biol. 107, 6–14. https://doi.org/10.1016/1047-8477(91)90025-R
973 Leidel, S., Delattre, M., Cerutti, L., Baumer, K., Gönczy, P., 2005. SAS-6 defines a protein
974 family required for centrosome duplication in C. elegans and in human cells. Nat. Cell
975 Biol. 7, 115–125. https://doi.org/10.1038/ncb1220
976 Leidel, S., Gönczy, P., 2003. SAS-4 Is Essential for Centrosome Duplication in C. elegans and
977 Is Recruited to Daughter Centrioles Once per Cell Cycle. Dev. Cell 4, 431–439.
978 https://doi.org/10.1016/S1534-5807(03)00062-5
979 Li, J., Kim, S., Kobayashi, T., Liang, F., Korzeniewski, N., Duensing, S., Dynlacht, B.D., 2012.
980 Neurl4, a novel daughter centriole protein, prevents formation of ectopic microtubule
981 organizing centres. EMBO Rep. 13, 547–553. https://doi.org/10.1038/embor.2012.40
982 Li, Wenjing, Yi, P., Zhu, Z., Zhang, X., Li, Wei, Ou, G., 2017. Centriole translocation and
983 degeneration during ciliogenesis in Caenorhabditis elegans neurons 36, 2553–2566.
984 https://doi.org/10.15252/embj.201796883
985 Lints, R., Hall, D.H., 2004. WormAtlas Hermaphrodite Handbook - Reproductive System -
986 Overview. WormAtlas. https://doi.org/10.3908/wormatlas.1.21
987 Magescas, J., Zonka, J.C., Feldman, J.L., 2019. A two-step mechanism for the inactivation of

988 microtubule organizing center function at the centrosome. Elife 8, 1–28.
989 https://doi.org/10.7554/eLife.47867.001
990 Malone, C.J., Misner, L., Le Bot, N., Tsai, M.-C., Campbell, J.M., Ahringer, J., White, J.G.,
991 2003. The C. elegans Hook Protein, ZYG-12, Mediates the Essential Attachment
992 between the Centrosome and Nucleus. Cell 115, 825–836.
993 https://doi.org/10.1016/S0092-8674(03)00985-1
994 Manandhar, G., Schatten, H., Sutovsky, P., 2005. Centrosome Reduction During
995 Gametogenesis and Its Significance1. Biol. Reprod. 72, 2–13.
996 https://doi.org/10.1095/biolreprod.104.031245
997 Mary, H., Rueden, C., Ferreira, T., 2016. KymographBuilder: Release 1.2.4 10.5281.
998 https://doi.org/10.5281/zenodo.591877
999 Matsuura, R., Ashikawa, T., Nozaki, Y., Kitagawa, D., 2016. LIN-41 inactivation leads to
1000 delayed centrosome elimination and abnormal chromosome behavior during female
1001 meiosis in Caenorhabditis elegans. Mol. Biol. Cell 27, 799–811.
1002 https://doi.org/10.1091/mbc.E15-10-0713
1003 Matthews, L.R., Carter, P., Thierry-Mieg, D., Kemphues, K., 1998. ZYG-9, A Caenorhabditis
1004 elegans Protein Required for Microtubule Organization and Function, Is a Component
1005 of Meiotic and Mitotic Spindle Poles. J. Cell Biol. 141, 1159–1168.
1006 https://doi.org/10.1083/jcb.141.5.1159
1007 Mikeladze-Dvali, T., von Tobel, L., Strnad, P., Knott, G., Leonhardt, H., Schermelleh, L.,
1008 Gönczy, P., 2012. Analysis of centriole elimination during C. elegans oogenesis.
1009 Development 139, 1670–1679. https://doi.org/10.1242/dev.075440
1010 Nechipurenko, I. V., Berciu, C., Sengupta, P., Nicastro, D., 2017. Centriolar remodeling
1011 underlies basal body maturation during ciliogenesis in Caenorhabditis elegans. Elife 6,
1012 1–12. https://doi.org/10.7554/eLife.25686
1013 Nelson, G.A., Lew, K.K., Ward, S., 1978. Intersex, a temperature-sensitive mutant of the
1014 nematode Caenorhabditis elegans. Dev. Biol. 66, 386–409.
1015 https://doi.org/10.1016/0012-1606(78)90247-6
1016 Nigg, E.A., Holland, A.J., 2018. Once and only once: Mechanisms of centriole duplication and
1017 their deregulation in diseases. Nat. Rev. Mol. Cell Biol. 19, 297–312.
1018 https://doi.org/10.1038/nrm.2017.127
1019 O'Rourke, S.M., Carter, C., Carter, L., Christensen, S.N., Jones, M.P., Nash, B., Price, M.H.,

1020 Turnbull, D.W., Garner, A.R., Hamill, D.R., Osterberg, V.R., Lyczak, R., Madison, E.E.,
1021 Nguyen, M.H., Sandberg, N.A., Sedghi, N., Willis, J.H., Yochem, J., Johnson, E.A.,
1022 Bowerman, B., 2011. A Survey of New Temperature-Sensitive, Embryonic-Lethal
1023 Mutations in C. elegans: 24 Alleles of Thirteen Genes. PLoS One 6, e16644.
1024 https://doi.org/10.1371/journal.pone.0016644
1025 Ohta, M., Desai, A., Oegema, K., 2017. How centrioles acquire the ability to reproduce. Elife
1026 6, 4–7. https://doi.org/10.7554/eLife.25358
1027 Pazdernik, N., Schedl, T., 2013. Introduction to Germ Cell Development in Caenorhabditis
1028 elegans. pp. 1–16. https://doi.org/10.1007/978-1-4614-4015-4_1
1029 Phillips, C.M., McDonald, K.L., Dernburg, A.F., 2009. Cytological Analysis of Meiosis in
1030 Caenorhabditis elegans. Methods Mol. Biol. 558, 171–195.
1031 https://doi.org/10.1007/978-1-60761-103-5
1032 Pierce, D.W., Hom-Booher, N., Otsuka, A.J., Vale, R.D., 1999. Single-molecule behavior of
1033 monomeric and heteromeric kinesins. Biochemistry 38, 5412–5421.
1034 https://doi.org/10.1021/bi9830009
1035 Pierron, M., Kalbfuss, N., Borrego-Pinto, J., Lénárt, P., Gönczy, P., 2020. Centriole foci persist
1036 in starfish oocytes despite Polo-like kinase 1 inactivation or loss of microtubule
1037 nucleation activity. Mol. Biol. Cell 31, 873–880. https://doi.org/10.1091/mbc.E19-06-
1038 0346
1039 Pimenta-Marques, A., Bento, I., Lopes, C.A.M., Duarte, P., Jana, S.C., Bettencourt-Dias, M.,
1040 2016. A mechanism for the elimination of the female gamete centrosome in Drosophila
1041 melanogaster. Science 353, aaf4866. https://doi.org/10.1126/science.aaf4866
1042 Pintard, L., Bowerman, B., 2019. Mitotic Cell Division in Caenorhabditis elegans. Genetics
1043 211, 35–73. https://doi.org/10.1534/genetics.118.301367
1044 Postma, M., Goedhart, J., 2019. PlotsOfData—A web app for visualizing data together with
1045 their summaries. PLOS Biol. 17, e3000202.
1046 https://doi.org/10.1371/journal.pbio.3000202
1047 Pruss, R.M., Mirsky, R., Raff, M.C., Thorpe, R., Dowding, A.J., Anderton, B.H., 1981. All
1048 classes of intermediate filaments share a common antigenic determinant defined by a
1049 monoclonal antibody. Cell 27, 419–428. https://doi.org/10.1016/0092-8674(81)90383-
1050 4
1051 Qiao, R., Cabral, G., Lettman, M.M., Dammermann, A., Dong, G., 2012. SAS-6 coiled-coil

1052 structure and interaction with SAS-5 suggest a regulatory mechanism in C. elegans
1053 centriole assembly. EMBO J. 31, 4334–4347. https://doi.org/10.1038/emboj.2012.280
1054 Sallee, M.D., Zonka, J.C., Skokan, T.D., Raftrey, B.C., Feldman, J.L., 2018. Tissue-specific
1055 degradation of essential centrosome components reveals distinct microtubule
1056 populations at microtubule organizing centers. PLOS Biol. 16, e2005189.
1057 https://doi.org/10.1371/journal.pbio.2005189
1058 Schumacher, J.M., Ashcroft, N., Donovan, P.J., Golden, A., 1998. A highly conserved
1059 centrosomal kinase, AIR-1, is required for accurate cell cycle progression and
1060 segregation of developmental factors in Caenorhabditis elegans embryos.
1061 Development 125, 4391–4402. https://doi.org/10.1242/dev.125.22.4391
1062 Serwas, D., Su, T.Y., Roessler, M., Wang, S., Dammermann, A., 2017. Centrioles initiate cilia
1063 assembly but are dispensable for maturation and maintenance in C. elegans. J. Cell Biol.
1064 216, 1659–1671. https://doi.org/10.1083/jcb.201610070
1065 Shirato, Y., Tamura, M., Yoneda, M., Nemoto, S.-I., 2006. Centrosome destined to decay in
1066 starfish oocytes. Development 133, 343–50. https://doi.org/10.1242/dev.02193
1067 Shiratsuchi, G., Takaoka, K., Ashikawa, T., Hamada, H., Kitagawa, D., 2015. <scp>RBM</scp>
1068 14 prevents assembly of centriolar protein complexes and maintains mitotic spindle
1069 integrity. EMBO J. 34, 97–114. https://doi.org/10.15252/embj.201488979
1070 Simerly, C., Manil-Ségalen, M., Castro, C., Hartnett, C., Kong, D., Verlhac, M.-H., Loncarek, J.,
1071 Schatten, G., 2018. Separation and Loss of Centrioles From Primordidal Germ Cells To
1072 Mature Oocytes In The Mouse. Sci. Rep. 8, 12791. https://doi.org/10.1038/s41598-018-
1073 31222-x
1074 Sluder, G., Miller, F.J., Lewis, K., 1993a. Centrosome Inheritance in Starfish Zygotes II:
1075 Selective Suppression of the Maternal Centrosome during Meiosis. Dev. Biol. 155, 58–
1076 67. https://doi.org/10.1006/dbio.1993.1006
1077 Sluder, G., Miller, F.J., Lewis, K., 1993b. Centrosome inheritance in starfish zygotes II:
1078 Selective suppression of the maternal centrosome during meiosis. Dev. Biol. 155, 58–
1079 67. https://doi.org/10.1006/dbio.1993.1006
1080 Spike, C., Meyer, N., Racen, E., Orsborn, A., Kirchner, J., Kuznicki, K., Yee, C., Bennett, K.,
1081 Strome, S., 2008. Genetic analysis of the Caenorhabditis elegans GLH family of P-
1082 granule proteins. Genetics 178, 1973–1987.
1083 https://doi.org/10.1534/genetics.107.083469

1084 Sugioka, K., Hamill, D.R., Lowry, J.B., McNeely, M.E., Enrick, M., Richter, A.C., Kiebler, L.E.,
1085 Priess, J.R., Bowerman, B., 2017. Centriolar SAS-7 acts upstream of SPD-2 to regulate
1086 centriole assembly and pericentriolar material formation. Elife 6, 1–25.
1087 https://doi.org/10.7554/eLife.20353
1088 Thauvin-robinet, C., Lee, J.S., Lopez, E., Herranz-pérez, V., Shida, T., Franco, B., Jego, L., Ye,
1089 F., Pasquier, L., Loget, P., Gigot, N., Aral, B., Lopes, C.A.M., St-onge, J., Bruel, A.,
1090 Thevenon, J., González-granero, S., Alby, C., Munnich, A., Vekemans, M., Huet, F., Fry,
1091 A.M., Saunier, S., Rivière, J., Attié-bitach, T., Garcia-verdugo, J.M., Faivre, L.,
1092 Mégarbané, A., Nachury, M. V, 2014. The oral-facial-digital syndrome gene C2CD3
1093 encodes a positive regulator of centriole elongation. Nat. Publ. Gr. 46.
1094 https://doi.org/10.1038/ng.3031
1095 von Tobel, L., Mikeladze-Dvali, T., Delattre, M., Balestra, F.R., Blanchoud, S., Finger, S., Knott,
1096 G., Müller-Reichert, T., Gönczy, P., 2014. SAS-1 Is a C2 Domain Protein Critical for
1097 Centriole Integrity in C. elegans. PLoS Genet. 10, e1004777.
1098 https://doi.org/10.1371/journal.pgen.1004777
1099 Winey, M., O'Toole, E., 2014. Centriole structure. Philos. Trans. R. Soc. B Biol. Sci. 369.
1100 https://doi.org/10.1098/rstb.2013.0457
1101 Woglar, A., Pierron, M., Schneider, F.Z., Jha, K., Busso, C., Gönczy, P., 2022. Molecular
1102 architecture of the C. elegans centriole. PLOS Biol. 20, e3001784.
1103 https://doi.org/10.1371/journal.pbio.3001784
1104 Wueseke, O., Zwicker, D., Schwager, A., Wong, Y.L., Oegema, K., Jülicher, F., Hyman, A.A.,
1105 Woodruff, J.B., 2016. Polo-like kinase phosphorylation determines Caenorhabditis
1106 elegans centrosome size and density by biasing SPD-5 toward an assembly-competent
1107 conformation. Biol. Open 5, 1431–1440. https://doi.org/10.1242/bio.020990
1108 Zhou, K., Rolls, M.M., Hall, D.H., Malone, C.J., Hanna-Rose, W., 2009. A ZYG-12-dynein
1109 interaction at the nuclear envelope defines cytoskeletal architecture in the C. elegans
1110 gonad. J. Cell Biol. 186, 229–241. https://doi.org/10.1083/jcb.200902101
1111

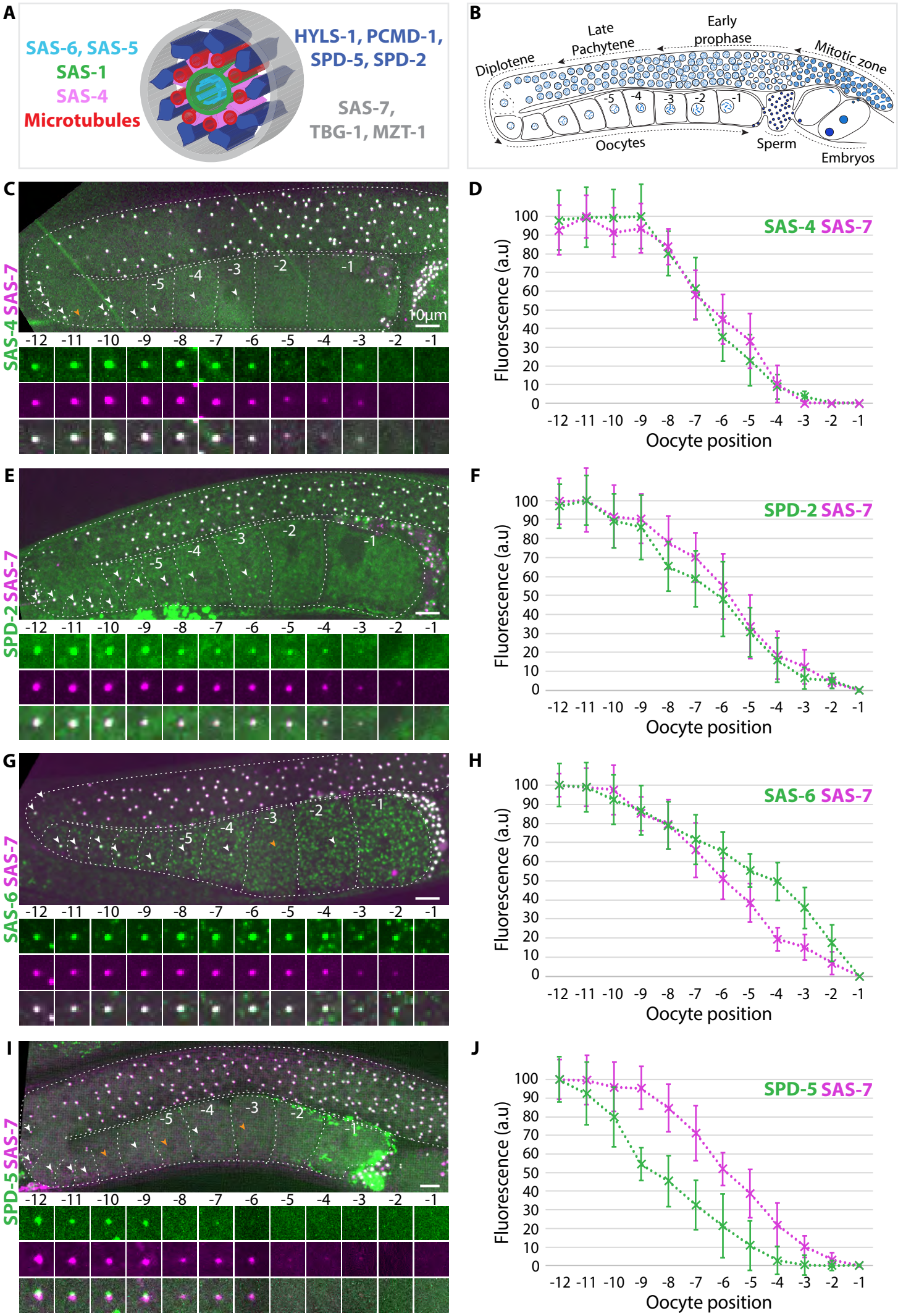
A
SAS-6, SAS-5
SAS-1
SAS-4
Microtubules
HYLS-1, PCMD-1,
SPD-5, SPD-2
SAS-7,
TBG-1, MZT-1
B
Diplotene
Late
Pachytene
Early
prophase
Mitotic zone
Oocytes
Sperm
Embryos
C
SAS-4 SAS-7
10µm
D
SAS-4 SAS-7
Fluorescence (a.u)
Oocyte position
E
SPD-2 SAS-7
F
SPD-2 SAS-7
G
SAS-6 SAS-7
H
SAS-6 SAS-7
I
SPD-5 SAS-7
J
SPD-5 SAS-7

FIGURE 1

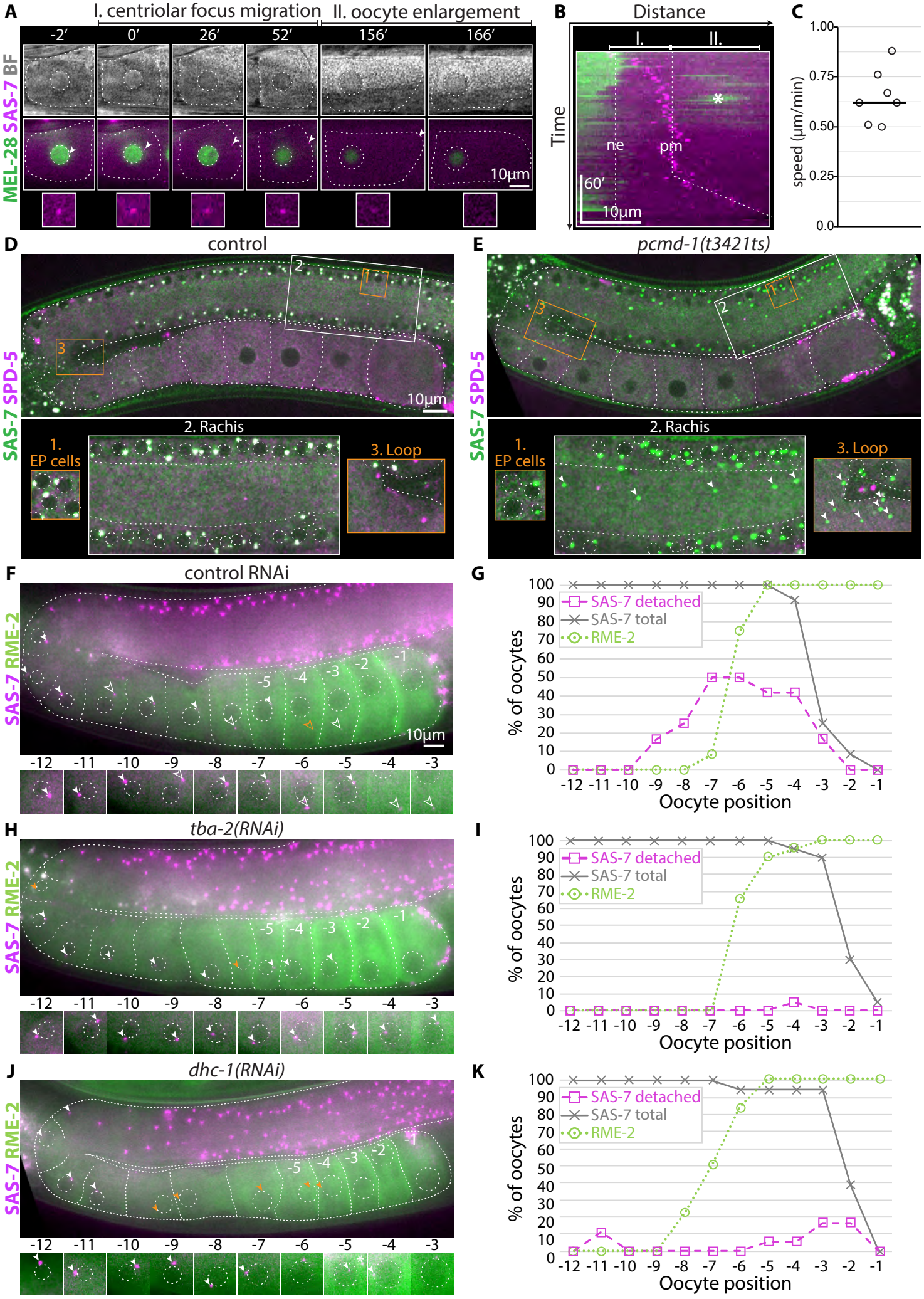
A
I. centriolar focus migration
II. oocyte enlargement
-2′
0′
26′
52′
156′
166′
MEL-28 SAS-7 BF
10µm
B
Distance
Time
I.
II.
ne
pm
60′
10µm
C
speed (µm/min)
1.00
0.75
0.50
0.25
0.0
D
control
SAS-7 SPD-5
10µm
2. Rachis
1. EP cells
3. Loop
E
pcmd-1(t3421ts)
SAS-7 SPD-5
2. Rachis
1. EP cells
3. Loop
F
control RNAi
SAS-7 RME-2
10µm
-12 -11 -10 -9 -8 -7 -6 -5 -4 -3
G
SAS-7 detached
SAS-7 total
RME-2
% of oocytes
Oocyte position
H
tba-2(RNAi)
SAS-7 RME-2
I
SAS-7 detached
SAS-7 total
RME-2
% of oocytes
Oocyte position
J
dhc-1(RNAi)
SAS-7 RME-2
K
SAS-7 detached
SAS-7 total
RME-2
% of oocytes
Oocyte position

Figure 2

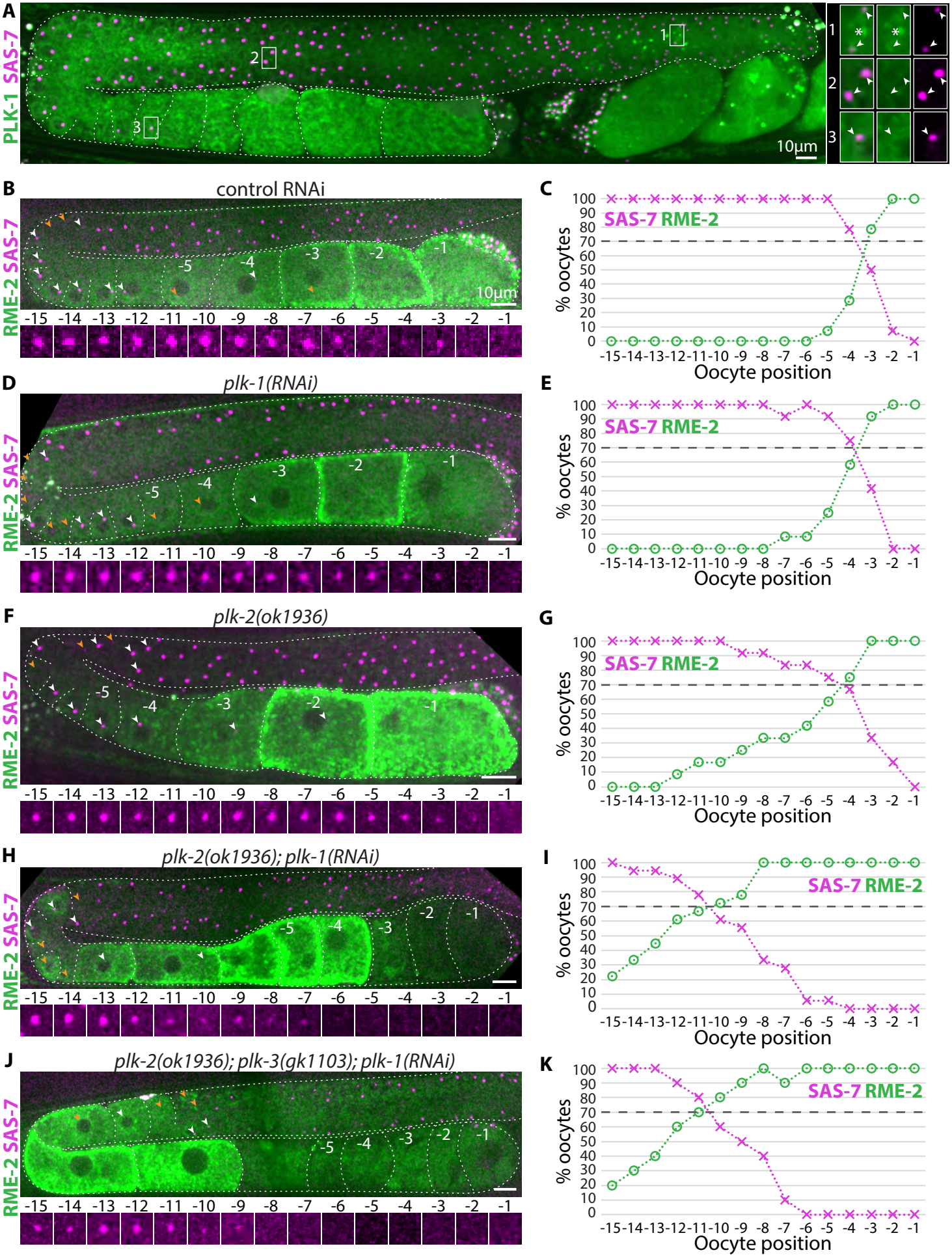
A
PLK-1 SAS-7
10µm
B
control RNAi
RME-2 SAS-7
10µm
C
SAS-7 RME-2
% oocytes
Oocyte position
D
plk-1(RNAi)
E
F
plk-2(ok1936)
G
H
plk-2(ok1936); plk-1(RNAi)
I
J
plk-2(ok1936); plk-3(gk1103); plk-1(RNAi)
K

FIGURE 3

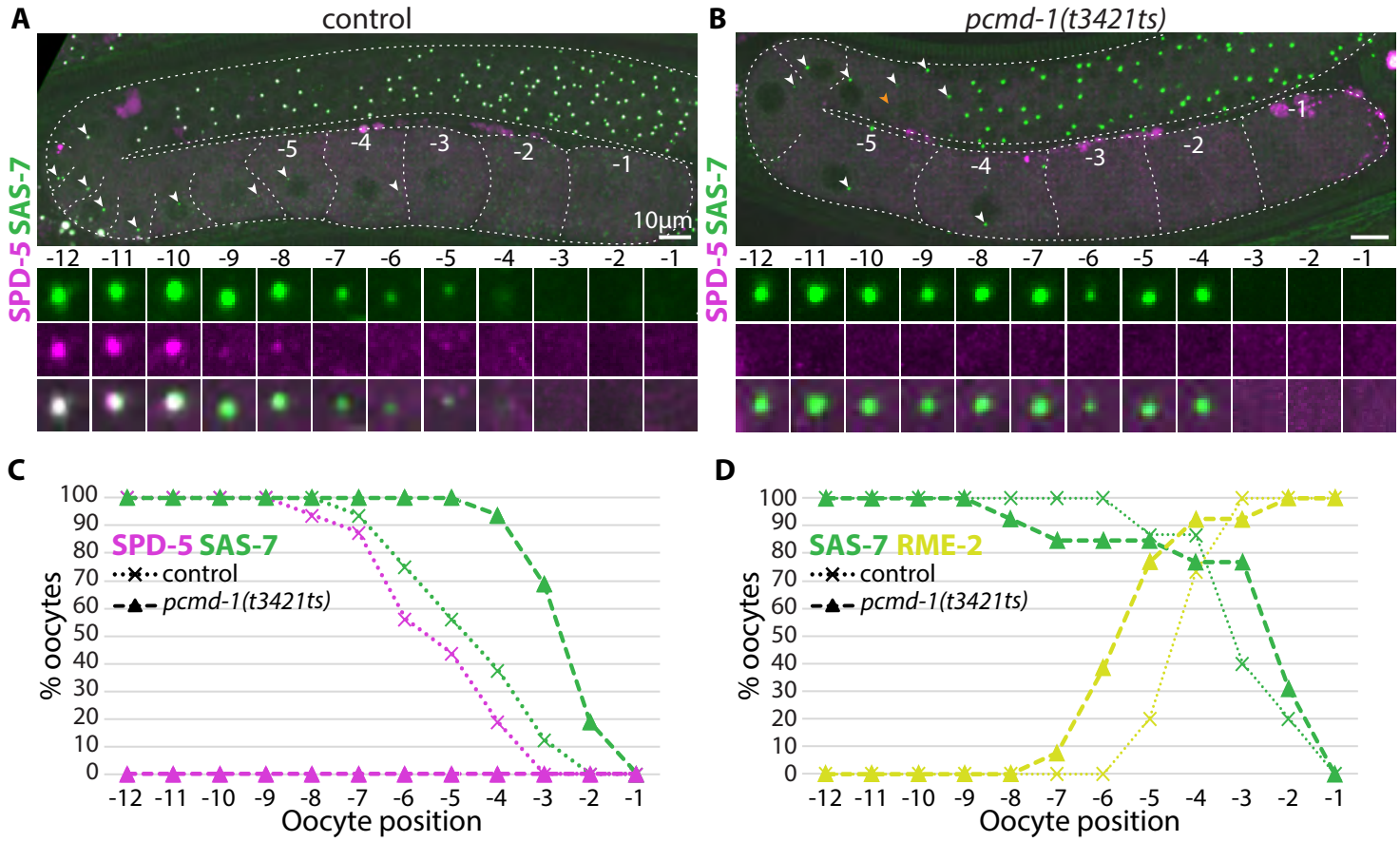
A
control
B
pcmd-1(t3421ts)
SPD-5 SAS-7
-5
-4
-3
-2
-1
10µm
-12 -11 -10 -9 -8 -7 -6 -5 -4 -3 -2 -1
C
SPD-5 SAS-7
control
pcmd-1(t3421ts)
% oocytes
Oocyte position
D
SAS-7 RME-2
control
pcmd-1(t3421ts)
% oocytes
Oocyte position

FIGURE 4

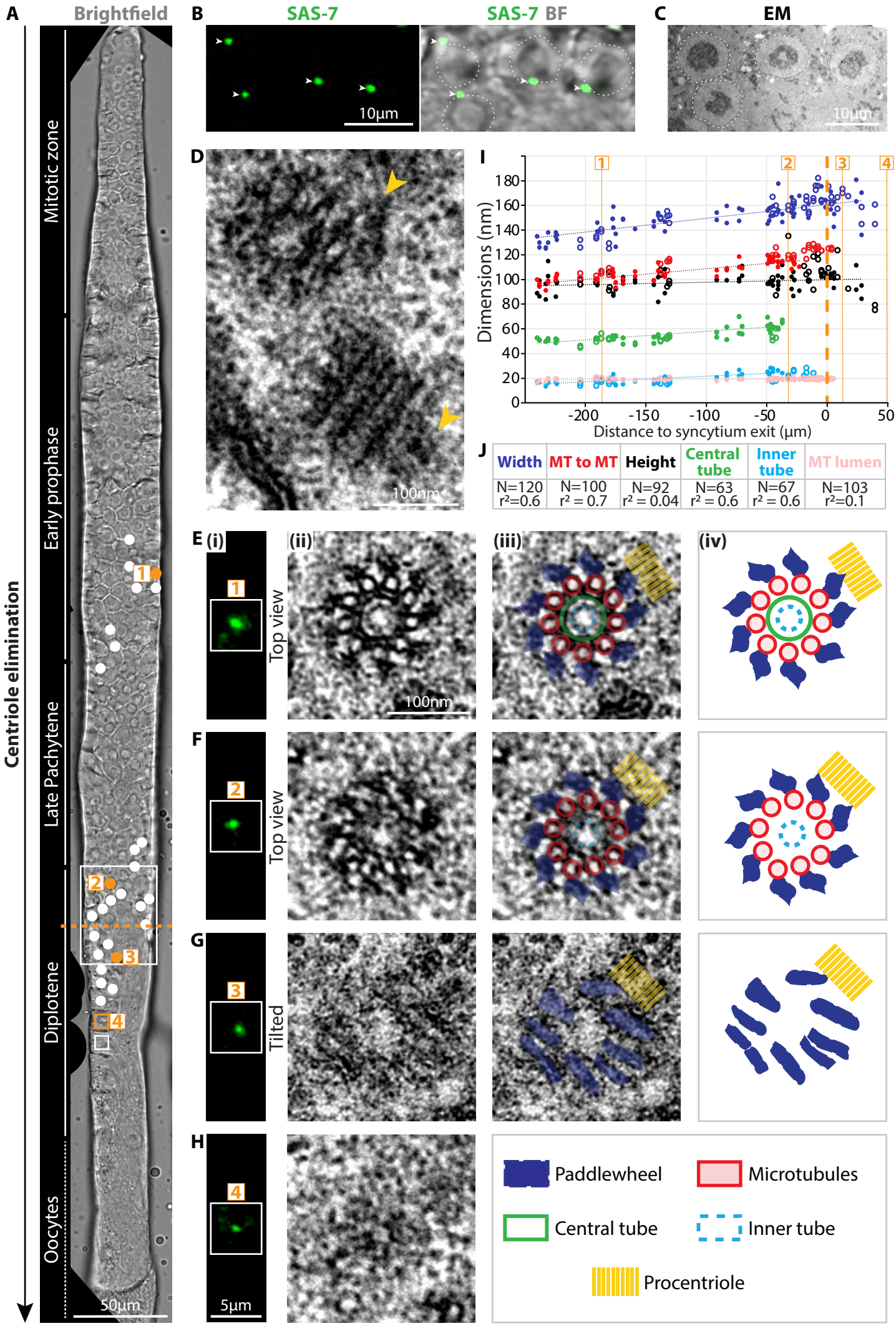
A
Brightfield
Centriole elimination
Mitotic zone
Early prophase
Late Pachytene
Diplotene
Oocytes
50µm
B
SAS-7
SAS-7 BF
10µm
C
EM
10µm
D
100nm
I
Dimensions (nm)
Distance to syncytium exit (µm)
J
Width N=120 r²=0.6
MT to MT N=100 r² = 0.7
Height N=92 r² = 0.04
Central tube N=63 r² = 0.6
Inner tube N=67 r² = 0.6
MT lumen N=103 r²=0.1
E (i) (ii) (iii) (iv)
Top view
100nm
F
Top view
G
Tilted
H
5µm
Paddlewheel
Microtubules
Central tube
Inner tube
Procentriole

FIGURE 5

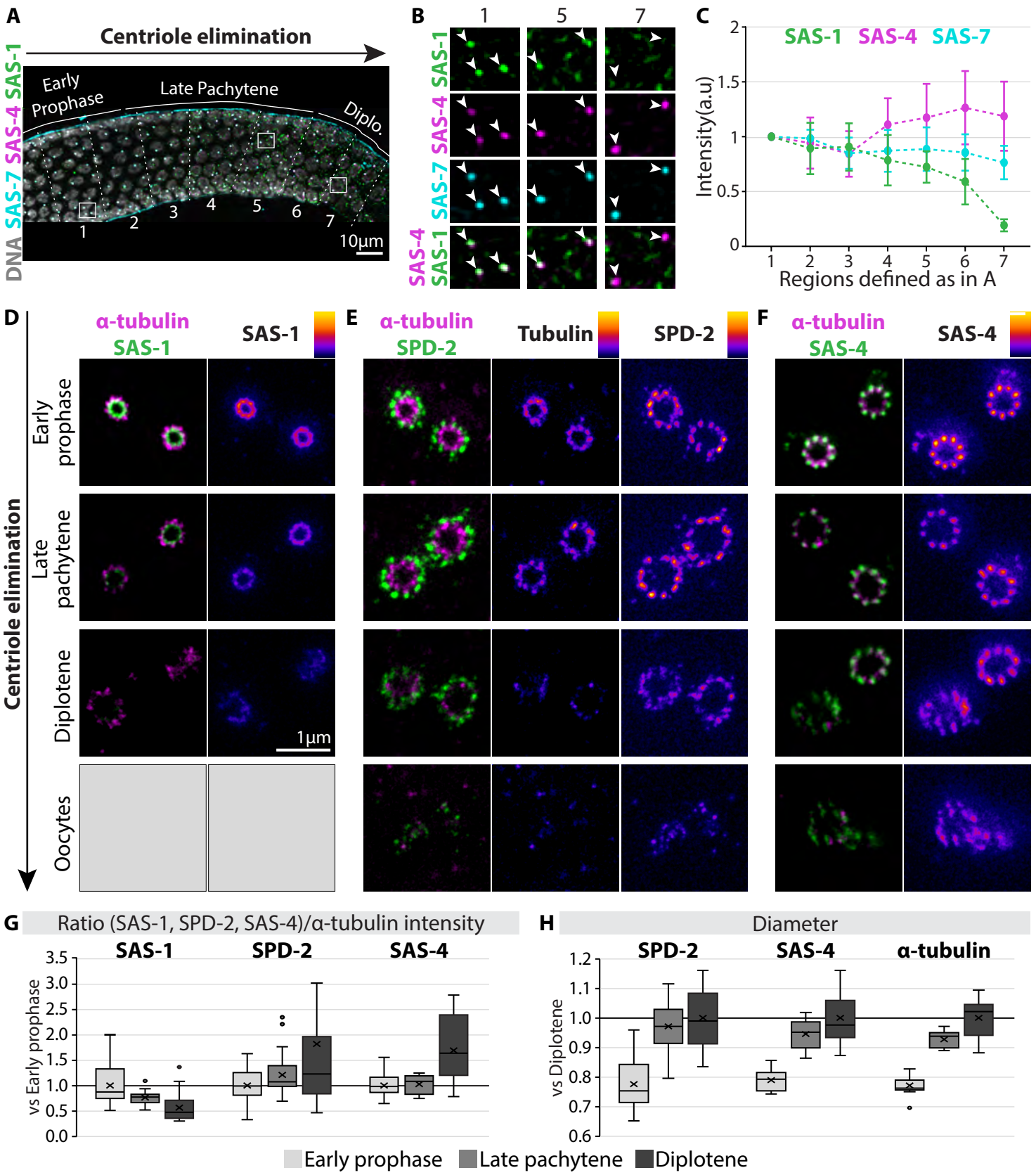
A
Centriole elimination
SAS-1
SAS-4
SAS-7
DNA
Early Prophase
Late Pachytene
Diplo.
1
2
3
4
5
6
7
10µm
B
1
5
7
SAS-1
SAS-4
SAS-7
SAS-4
SAS-1
C
SAS-1
SAS-4
SAS-7
Intensity(a.u)
Regions defined as in A
D
α-tubulin
SAS-1
SAS-1
Centriole elimination
Early prophase
Late pachytene
Diplotene
Oocytes
1µm
E
α-tubulin
SPD-2
Tubulin
SPD-2
F
α-tubulin
SAS-4
SAS-4
G
Ratio (SAS-1, SPD-2, SAS-4)/α-tubulin intensity
SAS-1
SPD-2
SAS-4
vs Early prophase
H
Diameter
SPD-2
SAS-4
α-tubulin
vs Diplotene
Early prophase
Late pachytene
Diplotene

FIGURE 6

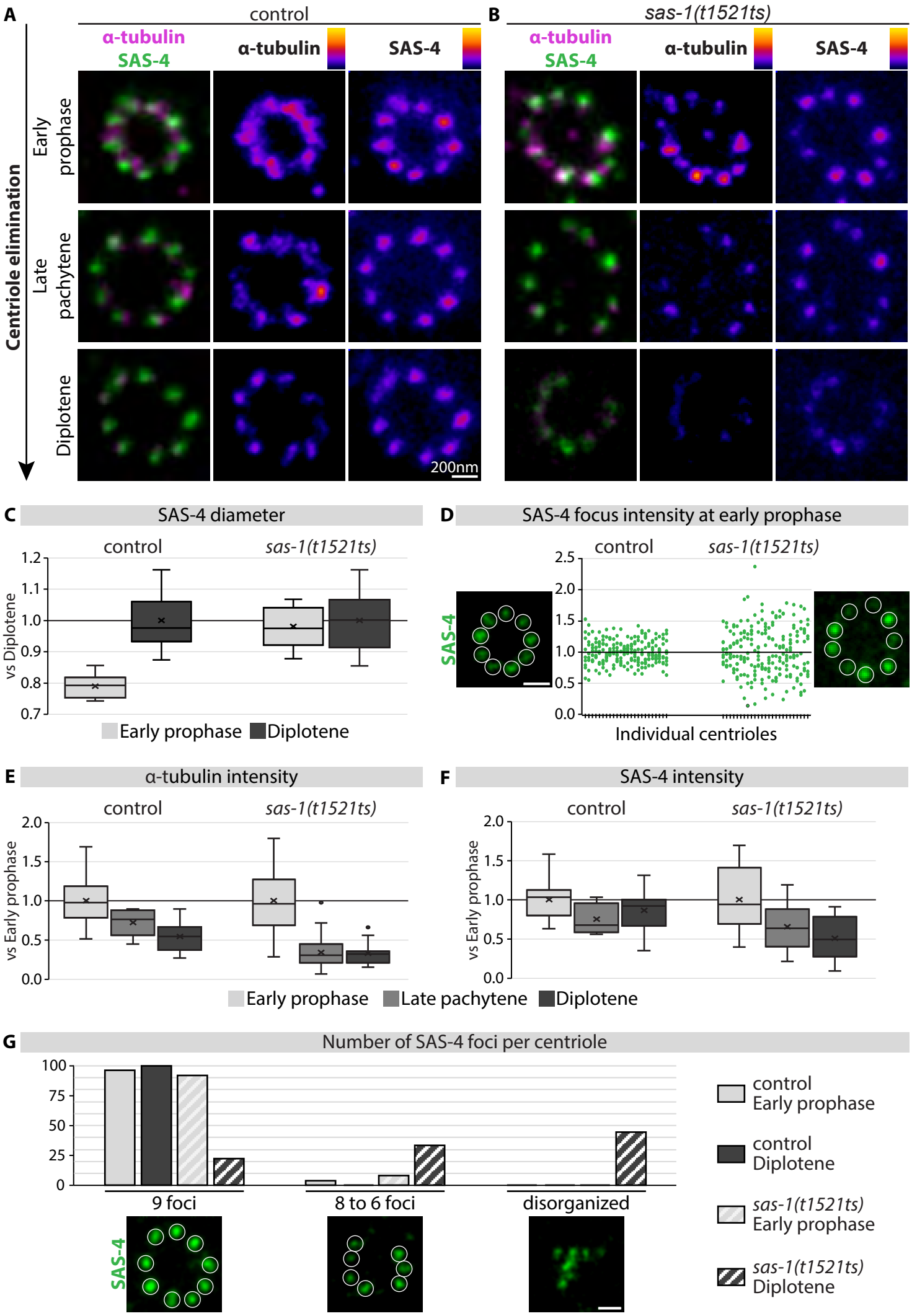
A
control
α-tubulin
SAS-4
α-tubulin
SAS-4
Centriole elimination
Early prophase
Late pachytene
Diplotene
200nm
B
sas-1(t1521ts)
α-tubulin
SAS-4
α-tubulin
SAS-4
C
SAS-4 diameter
control
sas-1(t1521ts)
vs Diplotene
1.2
1.1
1.0
0.9
0.8
0.7
Early prophase
Diplotene
D
SAS-4 focus intensity at early prophase
control
sas-1(t1521ts)
SAS-4
2.5
2.0
1.5
1.0
0.5
0.0
Individual centrioles
E
α-tubulin intensity
control
sas-1(t1521ts)
vs Early prophase
2.0
1.5
1.0
0.5
0.0
F
SAS-4 intensity
control
sas-1(t1521ts)
vs Early prophase
2.0
1.5
1.0
0.5
0.0
Early prophase
Late pachytene
Diplotene
G
Number of SAS-4 foci per centriole
100
75
50
25
0
9 foci
8 to 6 foci
disorganized
SAS-4
control
Early prophase
control
Diplotene
sas-1(t1521ts)
Early prophase
sas-1(t1521ts)
Diplotene

FIGURE 7